Pushing the Technology Envelope of Multi-Parametric Photoacoustic Microscopy

A Dissertation

Presented to the faculty of the School of
Engineering and Applied Science in partial
fulfillment of the requirements for the degree of

Doctor of Philosophy

---

by Tianxiong Wang

August 2018

DEPARTMENT OF BIOMEDICAL ENGINEERING

UNIVERSITY of VIRGINIA

Acknowledgments

I would like to thank my advisor, Dr. Song Hu, for his mentorship and the opportunity to work in his lab. Dr. Hu's experience and knowledge of photoacoustic microscopy has been a great resource throughout my graduate career. Without the support and guidance of Dr. Hossack and Dr. Periasamy, my research would have lacked the rigor and balance that has excited me throughout my graduate career. I would also like to thank my committee chair, Dr. Peirce-Cottler and Dr. Kapur for taking the time to discuss my research and provide valuable feedback. Your fresh perspectives on my project have enriched it.

I would like to thank all of the people who contributed to this research. My lab mates, especially Naidi Sun, Rui Cao, Dr. Bo Ning, Zhiqiang Xu, Fenghe Zhong, Yifeng Zhou and Yiming Wang. A special thanks to Dr. Adam Dixon for helping me with all the ultrasound related problems.

Abstract

Photoacoustic microscopy (PAM) is a hybrid imaging modality that combines the deep-penetration advantage of ultrasonic imaging with the high-resolution and high-contrast advantage of optical imaging. It detects the short pulsed laser induced photoacoustic waves, whose amplitudes reflect the localized laser energy absorption, to image the internal optical absorption distributions. Mathematically, the photoacoustic wave pressure can be described as $p_0 = \Gamma \eta_{th} \mu_a F$ where p_0 is the pressure, Γ is Grueneisen parameter, η_{th} is percentage that the abosorbed optical energy is converted into heat, μ_a is the optical absorption coefficient and F is the optical fluence (J/cm^2). Currently, conventional optical resolution PAM (OR-PAM) is facing two main challenges which limit its application in physiology studies, the highly anisotropic spatial resolution and slow imaging speed. This dissertation focuses on addressing these two problems and provides several potential solutions.

In OR-PAM, while the lateral resolution is determined by the optical focusing which can achieve micron level, the axial resolution determined by ultrasound detection bandwidth is usually at least one order of magnitude worse than the lateral resolution. Thus, compared to other optical imaging technique such as two photon microscopy (TPM) or optical coherence tomography (OCT), OR-PAM has poor performance in volumetric imaging with comparable axial and lateral resolution. This limitation strongly constraints the application of PAM in physiology and biology studies.

To address this issue, we present two potential methods. 1. OR-PAM with surface plasmon resonance (SPR) based ultrasound detector (SPR-PAM) that can achieve broad ultrasound detection bandwidth. Experimentally, an ultra-flat frequency response (±0.7 dB) from 680 kHz to 126 MHz has been examined. With the broad detection bandwidth, high spatial resolution (2.0 μm laterally and 8.4 μm axially) is achieved. 3D PA imaging of a melanoma cell with isotropic spatial

resolution is also presented. 2. OR-PAM with multi-angle illumination (MAI-PAM). With multi-angle illumination, PAM images from different view angles can be simultaneously acquired for multi-view deconvolution. We experimentally examine the system performance both in phantom and *in vivo*. The measurement results reveals that MAI-PAM achieved a high axial resolution of 3.7 μm, which is 10-fold higher than that of conventional PAM and approached the lateral resolution of 2.7 μm.

Conventional PAM employs pure mechanical scan and commercial 559-nm Raman pulsed laser with low pulse repetition rate (PRR) to realize oxygen saturation (sO_2) measurement. These two factors significantly limits the imaging speed of PAM. To address these problems, we realize a high speed multi-parametric PAM with A-line rate of 300-kHz by employing optical-mechanical hybrid scan mode and stimulated Raman scattering (SRS) based wavelength conversion method to generate 558-nm pulsed laser. Compared to conventional PAM, 20-fold imaging speed improvement is achieved. The system performance is examined both *in vitro* and *in vivo*. Employing two 600-kHz PRR pulsed lasers and a weakly focused ultrasound transducer with 250-μm focal zone diameter, we develop an ultra-high speed multi-parametric PAM with A-line rate of 1.2-MHz which further improves imaging speed by 6-fold over the 300-kHz high-speed PAM. The system is validated by performing side-by-side measurement comparison between our previously well-developed multi-parametric PAM and the ultra-high speed multi-parametric PAM.

Contents

List of Tables

List of Figures

Chapter 1

Introduction

1.1 General Introduction

Optical imaging is the use of light as an investigational imaging technique for medical applications. Compared to existing radiological techniques, optical imaging technology shows several advantages. As shown in Table 1.1 [1], optical imaging is based on non-ionizing illumination and exhibits excellent contrast and resolution. Optical imaging can also achieve good imaging depth, for example, two photon microscopy can achieve > 500 μm imaging depth in brain [2]. Moreover, optical imaging also provides functional measurement with low cost. Several optical imaging methods have been playing an important role in biology and physiology study. For example, confocal microscopy and two photon microscopy that can realize high resolution in three dimensions have been widely used in cell study and neuron science [3,4], optical coherence tomography (OCT) can realize high-resolution deep tissue imaging in scattering biological tissue has been widely used in ophthalmology study [5–7].

In the last decade, photoacoustic tomography (PAT) has been drawing increasing attention from various research communities, including imaging [8,9], chemistry [10], and biomedicine [11–15]. The term PAT refers to imaging that is based on the photoacoustic (PA) effect. As shown in Fig. 1.1(a), in PA imaging, illuminated by pulsed laser, the light energy is absorbed by molecules and

partially converted into heat. The heat then induces thermoelectric expansion and an initial pressure rise, which propagates as an acoustic wave. An broadband ultrasonic transducer or transducer array detects the acoustic wave to form an image, which maps the original optical energy deposition in the tissue [9].

Table 1.1 [1] Comparison of various medical imaging modalities

Characteristics	X-ray Imaging	Ultrasonography	MRI	Optical Imaging
Soft-tissue contrast	Poor	Good	Excellent	Excellent
Spatial resolution	Excellent	Good	Good	Mixed
Maximum Imaging depth	Excellent	Good	Excellent	Good
Function	None	Good	Excellent	Excellent
Nonionizing radiation	No	Yes	Yes	Yes
Data acquisition	Fast	Fast	Slow	Fast
Cost	Low	Low	High	Low

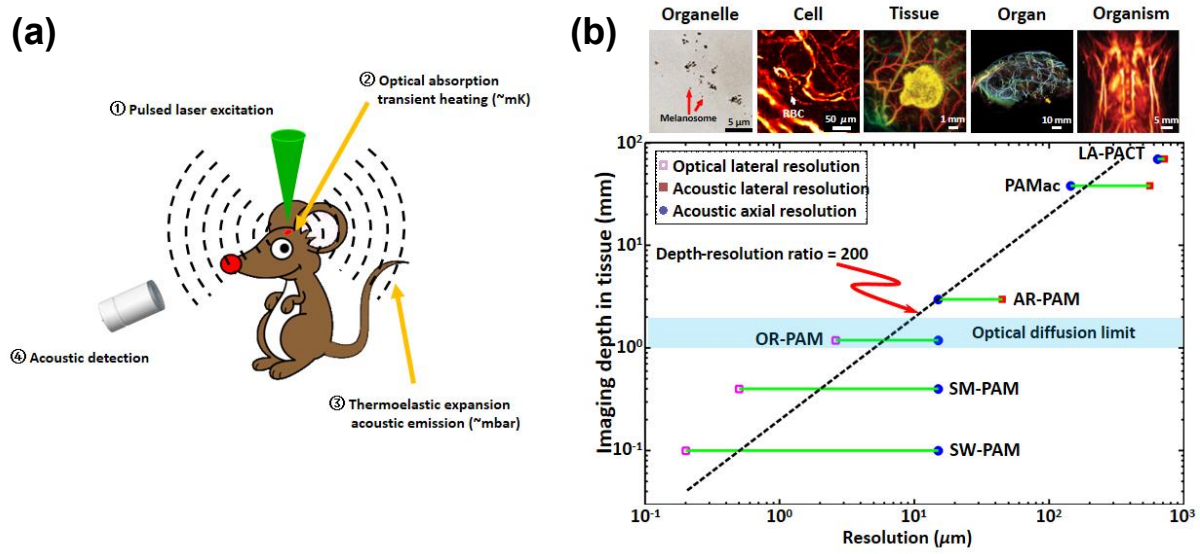

Fig. 1.1 Principle of photoacoustic imaging. (a) Principle of photoacoustic imaging. (b) Multiple types of photoacoustic imaging system. [16–20]

Table 1.2 [1] Comparison of optical coherence tomography (OCT), diffuse optical tomography (DOT), ultrasonography (US) operating at 5 MHz, and photoacoustic tomography (PAT)

Property	OCT	DOT	US	PAT
Contrast	Good	Excellent	Poor for early cancers	Excellent
Imaging depth	Poor (~ 1mm)	Good (~ 50mm)	Excellent and scalable (~ 60 mm)	Good and scalable
Resolution	Excellent (~0.01 mm)	Poor (~ 5mm)	Excellent and scalable (~ 0.3 mm)	Excellent and scalable
Speckle artifacts	Strong	None	Strong	None
Scattering coefficient	Strong (~10 mm^{-1})	Strong (~ 10 mm^{-1})	Weak (~0.03 mm^{-1})	Mixed

Compared with other optical imaging and ultrasound imaging techniques, PAT has its unique advantages. (i) Due to the low scattering and attenuation of ultrasound in tissue, PAT can break through the optical diffusion limit [15]. (ii) PAT that based on different measurement scheme and image reconstruction method can realize multi-scale imaging of biological structures with high resolution. (iii) PAT can reveal rich optical contrasts according to chemical composition by selecting different excitation optical wavelength. (iv) PAT images optical absorption with very high sensitivity, two orders of magnitude greater than those of confocal microscopy and optical coherence tomography [21]. (v) In PAT, the background tissue with no optical absorption generates zero background signal and thus background-free detection can be realized. (vi) For a specific imaging target, there is always an optimum wavelength that maximize its absorption while there are much fewer molecules are fluorescent. (vii) PAT can be applied to measure functional

parameters beyond biological structure. For example, by using dual-wavelength optical excitation, oxygen-saturation (sO_2) can be measured effectively [22]. The comparison between PAT and other imaging techniques is shown in Table 1.2 [1].

As shown in Fig. 1.1(b), there are multiple types of PA imaging system due to different imaging method. The most widely used are optical-resolution photoacoustic microscopy (OR-PAM), acoustic-resolution photoacoustic microscopy (AR-PAM) and photoacoustic computed tomography (PACT). In OR-PAM, a focused laser beam is employed for PA excitation and the lateral resolution is determined by the focal spot size of laser beam [19,23]. Mathematically, the lateral resolution can be expressed as $r = 0.51\frac{\lambda}{NA}$ where r is lateral resolution, λ is laser wavelength and NA is numerical aperture of objective lens. For example, illuminating with 532-nm beam with a 0.1 NA optical objective, the imaging lateral resolution can achieve 2.7 μm which can resolve single red blood cell *in vivo*. The axial resolution is determined by the equation $R_a = 0.88c/\Delta f$ [24], where R_a is the axial resolution, c is the speed of sound and Δf is the 6-dB bandwidth of ultrasound transducer. Due to optical scattering and absorption, the imaging depth is typically limited to be ~ 1 mm. To acquire an image, OR-PAM needs to perform point-by-point scanning of the optical focal spot and thus the imaging speed is determined by the scanning speed. AR-PAM typically uses weakly focused or unfocused light to excite PA signal and uses a focused ultrasound transducer to detect the signal [25,26]. The lateral resolution is determined by the ultrasound focal spot size which typically is several tens of micron while the axial resolution is as same as that of OR-PAM. Due to the weak scattering and absorption of ultrasound inside tissue, the imaging depth of AR-PAM can achieve several millimeters. To acquire an image, AR-PAM needs to perform point-by-point scanning of transducer focal spot and thus the imaging speed is limited by the scanning speed. Similar to AR-PAM, PACT employs unfocused light to excite PA

signal, however, instead of using a single ultrasound transducer, PACT uses transducer array for PA signal detection [27–29]. The lateral resolution of PACT is determined by the width of each transducer element and transducer bandwidth which typically results in range of several hundred micron, the axial resolution is determined by the bandwidth of transducer which typically ranges from several tens of micron to several hundreds of micron. Unlike OR-PAM or AR-PAM, in PACT, each transducer element has a large acceptance angle within the field of view, and a PA image can be reconstructed by merging data from all transducer elements. Thus PACT does not need point-by-point scanning and the imaging speed is typically faster than OR-PAM and AR-PAM.

OR-PAM has been widely used in tissue-scale imaging [16,30,31]. The optics defined micron-level lateral resolution enables OR-PAM to resolve single capillary which is usually in the scale of ~10 μm. Moreover, PAM is heretofore the only technique that allows *in vivo* label-free quantification of the metabolic rate of oxygen (MRO_2) [32,33], a gold-standard metabolic index with extreme importance in cancer and ischemia. By distinguishing the oxy- and deoxy-hemoglobin (HbO_2 and HbR) via their optical absorption spectra, dual-wavelength PAM enables wide-field mapping of total hemoglobin centration (C_{Hb}) [34] and oxygen saturation (sO_2) down to the capillary level. By analyzing the fluctuation of photoacoustic signals, PAM can also detect the blood flow speed in feeding arteries and draining veins [35]. Combining the multiple anatomical and functional parameters permits the derivation of the total MRO_2 in closed-circulation systems.

1.2 Recent Development of Photoacoustic Microscopy

During last decade, both the application and the technique of PAM has been developed significantly. PAM has been employed to realize imaging from organelle level to tissue level. Yao *et al*. invented ultra-violet photoacoustic microscopy (UV-PAM) to realize *in vivo* cell nuclei imaging without staining by employing a ultra-violet pulsed laser [36,37]. In UV-PAM, the image contrast relies on the difference in light absorption between nucleic acids and cytoplasmic proteins, such as thymus DNA and glutamate dehydrogenase. The ratio of the absorption coefficient of thymus DNA to that of glutamate dehydrogenase achieves high value when the excitation wavelength ranges from 245 nm to 275 nm. By using a water-immersion optical objective with a 1.23 NA, Zhang *et al*. developed a sub-wavelength-resolution photoacoustic microscopy (SW-PAM) which achieves 220-nm lateral resolution at 532 nm and measured melanin distribution of a black mouse ear with focal depth of ~10 μm [20]. According to their results, single melanosomes can be clearly identified. Wang *et al*. developed single-RBC PA flowoxigraphy (FOG) [38], which allows label-free real-time reflection-mode imaging of single flowing RBCs delivering oxygen to tissue *in vivo*. He *et al*. developed a dual-wavelength PA flow cytography technology [39]. The system employs 532 nm and 1064 nm as excitation wavelengths and obtains images of single circulating tumor cells (CTCs) flowing in both arteries and veins on the fly. By combining the two images acquired by 532 nm and 1064 nm respectively, single CTCs can be monitored effectively inside blood vessels. Ning *et al*. developed a multi-parametric PAM platform [40,41]. By analyzing both the sO_2-encoded spectral dependence and the flow-induced temporal decorrelation of PA signals generated by the raster-scanned mouse ear vasculature, they demonstrated simultaneous wide-field PAM of microvascular diameter, oxygen saturation (sO_2) and blood flow down to the capillary level *in vivo*. Hajireza *et al*. developed a non-interferometric PA remote

sensing microscopy (PARS) which is a pure optical PAM [42,43]. Illuminated by excitation beam, PA wave is generated inside the tissue and the PA wave will modulate the localized refractive index. PARS microscopy employs another non-interferometric probe beam to detect the localized refractive index change by measuring its reflectivity. In this case, PA signal can be detected without any ultrasound coupling. To extend depth of field (DoF) in PAM, Jiang *et al*. developed a Bessel-beam PAM (BB-PAM) which employs Bessel-beam rather than Gaussian beam as excitation beam [44]. The DoF is measured to be 483 μm by imaging a carbon fiber network. According to their results, the DoF of BB-PAM is about 7 times that of a Gaussian beam PAM.

1.3 Motivation and Dissertation Outline

Currently, the development of OR-PAM is facing two main challenges, the poor axial resolution and long image acquisition time. As mentioned in 1.1, in OR-PAM, the axial resolution is typically an order of magnitude worse than the lateral resolution, leading to the strong resolution anisotropy and poor volumetric imaging quality. Several techniques has been invented to solve this problem including applying optics based ultrasound detector to provide wide ultrasound detection bandwidth, exploring nonlinear optical absorption to limit the nonlinear PA generation volume and acquire image with multi-angle illumination with appropriate reconstruction algorithm. For the imaging speed issue, conventional PAM acquires an image by performing pure mechanical scan which significantly limits the imaging speed. Moreover, the lack of commercial available high-speed laser in 558-nm limits the ability of high-speed functional measurement. A lot of physiology processes happens in short time duration. For example, the brain response to external stimulation happens with several seconds. Conventional PAM with long image acquisition time

cannot provide sufficient time-resolution to monitor the transient change. From chapter 2 to chapter 5, we will introduce several methods to address these two problems.

In chapter 2, we will introduce an implementation of PAM, which capitalizes on the effect of surface plasmon resonance (SPR) for optical detection of ultrasound. The SPR sensor in our all-optical PAM has shown, experimentally, a linear response to the acoustic pressure from 5.2 kPa to 2.1 MPa, an ultra-flat frequency response (±0.7 dB) from 680 kHz to 126 MHz, and a noise-equivalent pressure sensitivity of 3.3 kPa. With the broad detection bandwidth, our SPR-PAM has achieved high spatial resolution (2.0 μm laterally and 8.4 μm axially). Three-dimensional high-resolution imaging of a single melanoma cell is demonstrated.

In chapter 3, we will introduce a PAM with micron-level spatial resolution in all three dimensions (3D). With multi-angle illumination, PAM images from different view angles can be simultaneously acquired for multi-view deconvolution, without the rotation of imaging target. Side-by-side comparison of this multi-angle-illumination PAM (MAI-PAM) and conventional PAM, which share the same ultrasonic detector, was performed in both phantoms and live rodents. The phantom study showed that MAI-PAM achieved a high axial resolution of 3.7 μm, which was 10-fold higher than that of conventional PAM and approached the lateral resolution of 2.7 μm. Further, the *in vivo* study demonstrated that MAI-PAM was able to image the micro-vasculature in 3D with isotropic resolution.

In chapter 4, we will introduce the development of a new generation of multi-parametric PAM. Capitalizing on a self-developed high-repetition dual-wavelength pulsed laser and an optical-mechanical hybrid-scan configuration, this innovative technique has achieved an unprecedented A-line rate of 300-kHz, leading to a 20-fold increase in the imaging speed over our previously

reported multi-parametric PAM that is based on pure mechanical scanning. The performance of the high-speed multi-parametric PAM has been examined both *in vitro* and *in vivo*. Simultaneous PAM of microvascular C_{Hb}, sO_2, and cerebral blood flow (CBF) in absolute values over a ~3-mm-diameter brain region of interest can be accomplished within 10 minutes.

In chapter 5, we will introduce the development of an ultra-high speed multi-parametric PAM with A-line rate of 1.2-MHz. Compared to the 300-kHz PAM introduced in chapter 4, we upgrade the laser pulse repetition rate (PRR) from 300-kHz to 1.2-MHz and employ a weakly focused ultrasound transducer with focal diameter of 250-μm. Combining these two factors leads to 6-fold imaging speed improvement over the 300-kHz PAM. Moreover, the system adapted a resonant optical scanner with scan frequency of 12 kHz. This triples the upper limit of measurable flow speed which is determined by the time interval between adjacent A-lines in one B-scan. To validate the system, in vivo PAM of mouse brain is performed by using both the ultra-high speed multi-parametric PAM and our well-developed conventional PAM. Side-by-side comparison between measurments results acquired by both systems is performed. The structure image shows comparable quality and the functional measurement of sO_2 and CBF matches each other. This demonstrates the measurement validity of ultra-high speed multi-parametric PAM.

In chapter 6, we will discuss limits of the above introduced system and related future work.

Chapter 2

All Optical Photoacoustic Microscopy Based On Plasmonic Detection of Broadband Ultrasound

2.1 Introduction

Combining optical contrast and acoustic penetration, PAM has attracted increasing attention in biomedicine [9]. In optical-resolution PAM, sub-micron lateral resolution has been achieved through tight optical focusing [45]. By contrast, the axial resolution is usually limited by the bandwidth of ultrasonic detection. For instance, the axial resolution of our recently reported multi-parametric PAM is 46.4 μm [41], which is more than an order of magnitude coarser than the optically defined lateral resolution (2.7 μm). To reduce the anisotropy in spatial resolution, there is an increasing number of research focusing on broadband ultrasound detection in PAM. With a broadband piezoelectric ultrasonic transducer (3-dB receiving-only bandwidth: 100 MHz), the axial resolution of PAM has been refined to 9.5 μm and can be slightly improved to 7.6 μm by deconvolution, providing sufficient signal-to-noise ratio (SNR) [24]. Although encouraging, the broad frequency coverage is accompanied by a high central frequency (125 MHz), which results in reduced sensitivity to the relatively low-frequency (i.e., <75 MHz) components.

In this chapter, We report a SPR-based strategy for optical detection of the broadband photoacoustic signal generated in PAM. The amplitude and frequency responses of the SPR sensor are examined experimentally. Providing an easy-to-implement solution to achieve linear amplitude response (R^2 = 0.99 from 5.2 kPa to 2.1 MPa) and ultra-flat frequency response (±0.7 dB from 680 kHz to 126 MHz) to acoustic pressure, this innovation complements existing all-optical PAM based on the micro-ring resonator [46,47] and Fabry-Perot polymer film [48].

2.2 Principle and System Setup

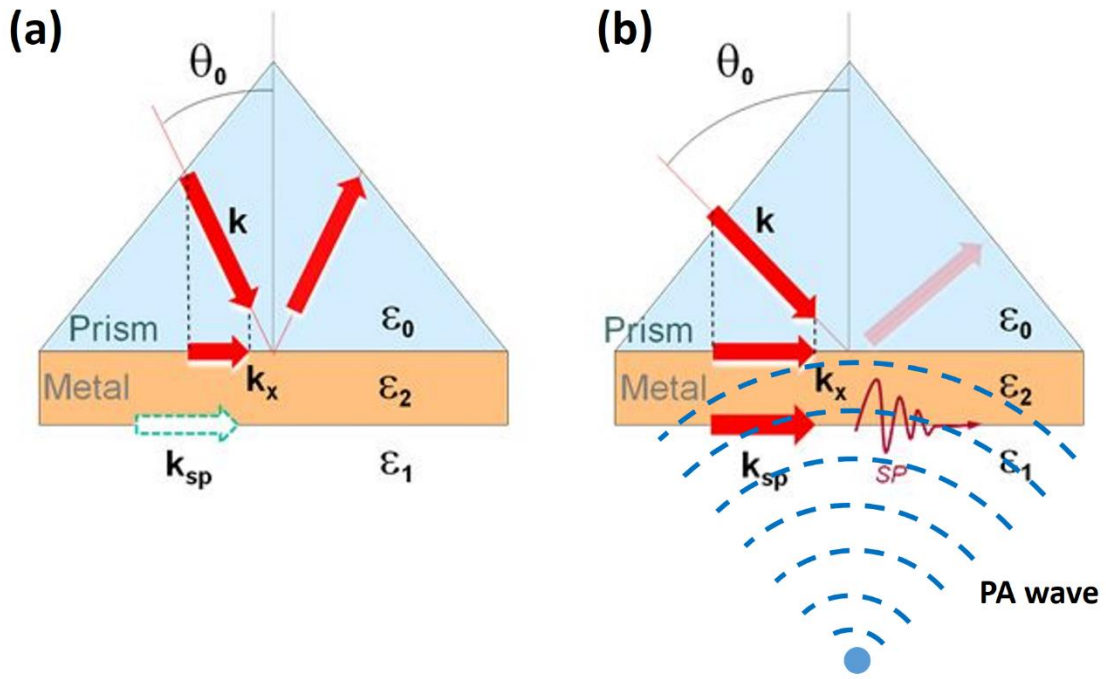

Fig. 2.1 Principle of surface plasmon resonance based ultrasound detector. k, wave vector of incident light; k_x, the x component of incident light wave vector; k_{sp}, wave vector of surface plasmon wave; PA, photoacoustic; ε_0, ε_1, ε_2, dielectric constant of prism, water and metal respectively.

As shown in Fig. 2.1(a), the essential of the SPR-based acoustic sensor in our all-optical PAM system lies in the interaction between the laser-excited acoustic wave and the surface plasmon wave (SPW). The SPW is an electromagnetic wave induced by the oscillation of charge density at a metal-dielectric interface. When the wave vector of the incident *p*-polarized light matches that of the SPW, i.e. $k_x = k_{sp}$ the resonant oscillation occurs and significant optical energy is coupled into the SPW, yielding reduced reflectance. As shown in Fig. 2.1(b), this resonance condition can be disturbed by the photoacoustic wave, when it propagates in the coupling liquid (e.g., water in our case) that is adjacent to the thin layer of metal (tens of nanometers). Specifically, the acoustic pressure-induced change in the refractive index of water leads to a shift in the resonant wavelength of the SPW at the metal-dielectric interface, thereby modulating the light-plasmon coupling and reflectance. By monitoring the intensity of the reflected light, the time-resolved photoacoustic signal can be derived. The frequency bandwidth of the SPR sensor is fundamentally limited by the dimension of the SPW field and can be as broad as GHz [49]. Indeed, acoustic signals on the scale of sub-nanosecond have been detected experimentally [50].

As shown in Fig. 2.2, our SPR-PAM utilizes an optical parametric oscillator (OPO)-based pulsed laser (NT242, Ekspla; pulse duration: 4.4 ns; repetition rate: 1 kHz) for photoacoustic excitation. The laser beam is expanded by a lens pair (LB1761 and LB1904, Thorlabs), reflected by a z-fold mirror set (BB1-E02, Thorlabs), and focused by a doublet (AC127-025-A, Thorlabs) into the imaging target placed on a glass slide. A continuous-wave semiconductor laser (OBIS 785 LX, Coherent; wavelength: 785 nm) is used for SPR sensing. The near-infrared wavelength of 785 nm is selected because the SPR sensitivity increases with the probe wavelength but insignificantly beyond 750 nm [51,52]. Since SPW can only be excited by p-polarized light, whose polarization is parallel to the incident plane [53], the *p*-polarization component of the probe beam is selected

by a polarizing beamsplitter (PBS102, Thorlabs), attenuated by a neutral-density filter (NDC-25C-2M, Thorlabs), focused through a lens (LB1779-B, Thorlabs), and reflected by a mirror (BB1-E03, Thorlabs) onto the bottom of a glass prism (47-275, Edmund Optics).

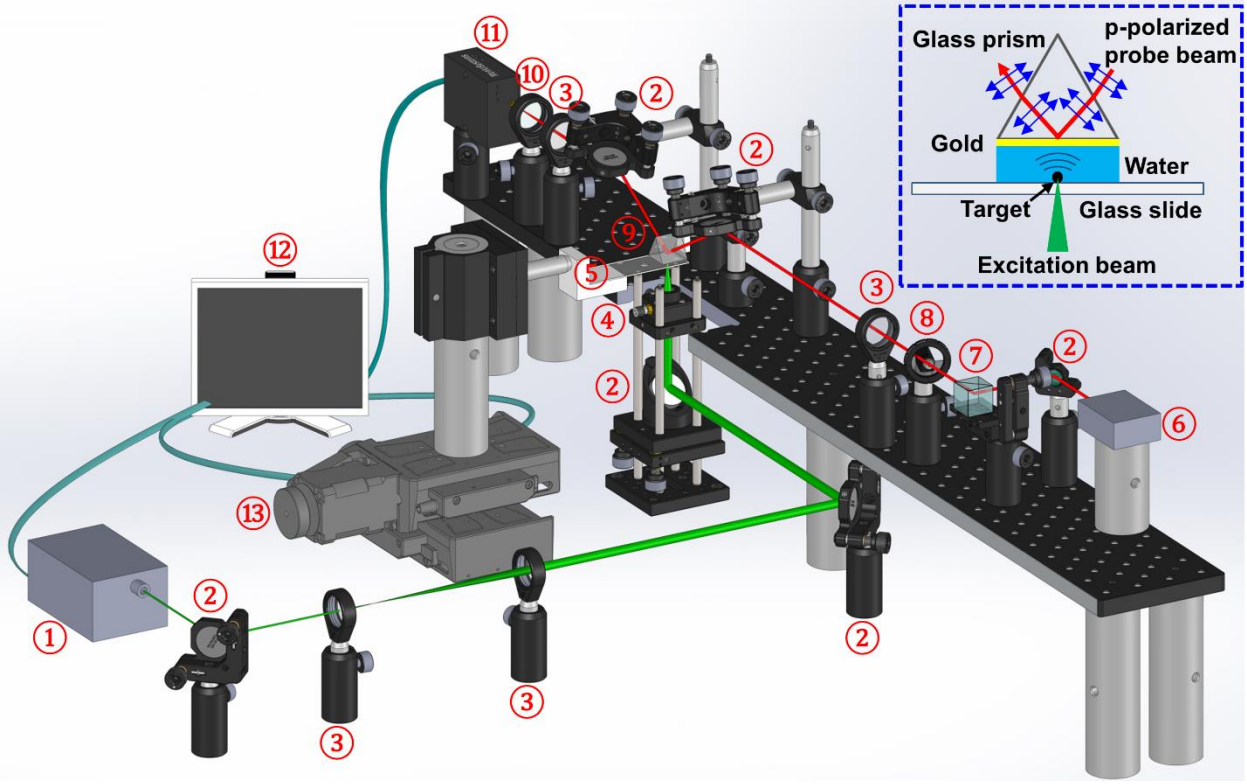

Fig. 2.2 Schematic of the SPR-PAM. ① pulsed excitation laser, ② mirror, ③ lens, ④ doublet mounted on a 2D translation stage, ⑤ imaging target placed on a glass slide, ⑥ continuous-wave probe laser, ⑦ polarizing beamsplitter, ⑧ neutral-density filter, ⑨ prism, ⑩ long-pass optical filter, ⑪ photodetector, ⑫ control and data acquisition system, and ⑬ scanning stages.

Our SPR sensor adopts the established Kretschmann configuration (see the boxed blow-up region in Fig. 2.2), which consists of three different media (i.e., water, gold, and glass). A thin film of gold is deposited on the bottom of the glass prism using an electron-beam evaporator. A drop of water is sandwiched between the imaging target and the gold film for acoustic coupling. The optimum thickness of the gold film and incident angle of probe beam are determined by numerical simulation. For each film thickness value, we calculated the normalized change in the light

reflectance at the gold-glass interface (ΔR/R) in response to a certain acoustic pressure (e.g., 10 kPa in the simulation) when the incident angle changes from 48 degrees to 55 degrees and extracted the maximum value as the achievable ΔR/R value at this thickness. Based on our simulation (Fig. 2.3), $\Delta R/R$ peaks when the thickness of gold film is 46.5nm and incident angle of the probe beam is 52.44 degrees. With this guidance, the mirror before the prism is carefully adjusted to maximize the SPR sensitivity.

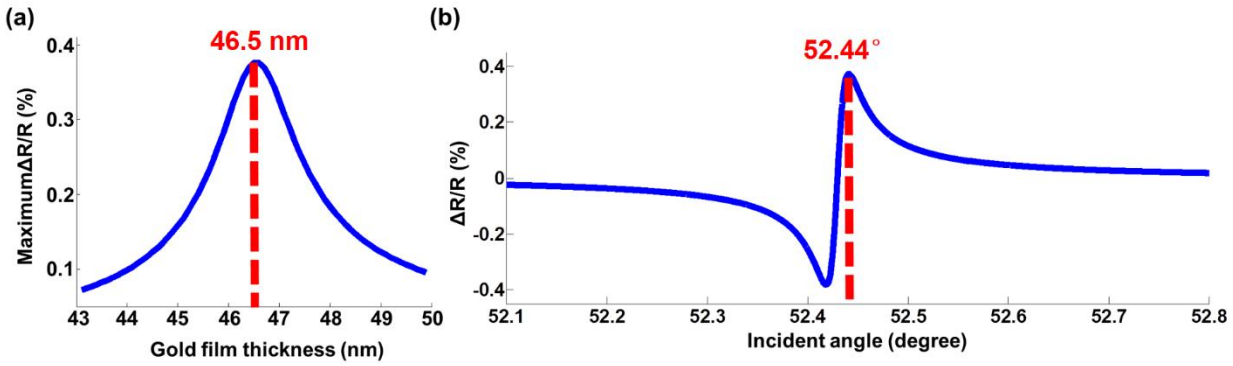

Fig. 2.3 Film thickness and incident angle-dependent SPR sensitivity. (a) The maximum achievable normalized change in the light reflectance at the gold-glass interface ($\Delta R/R$) in response to a 10-kPa acoustic pressure peaks when the film thickness of gold film is 46.5nm, the minimum achievable reflectance reaches deep simultaneously. (b) Under the condition of 46.5 nm thickness of gold film, $\Delta R/R$ in response to a 10-kPa acoustic pressure peaks when the incident angle is 52.44 degrees.

The SPR-modulated probe beam is then reflected by a mirror (BB1-E03, Thorlabs), focused by a lens (LB1471-B, Thorlabs), purified by a long-pass optical filter (FEL0700, Thorlabs), captured by a high-sensitivity photodetector (FPD510-FV, Thorlabs), and sampled by a waveform digitizer (ATS9350, AlazarTech) for image processing. Raster scanning the target-loading glass slide with

a two-axis linear stage (PLS-85, PI miCos) allows the acquisition of a three-dimensional (3D) PAM image.

2.3 Results

The performance of our SPR-PAM was thoroughly examined. The frequency response of the SPR-based acoustic sensor was characterized and compared with that of seven piezoelectric ultrasonic transducers centered at different frequencies [Fig. 2.4(a)]. Due to the limited space in the SPR-PAM, photoacoustic excitation optics and the glass slide beneath the prism were removed. Submerged in the water tank, each transducer was driven with an impulse generated by a pulser-receiver (5800PR, Olympus) to emit an acoustic pulse onto the gold-water interface. The acoustic wave modulated the light-plasmon coupling was detected by the SPR sensor, the echo wave from the interface was picked up by the same transducer. The frequency response of the transducer ($F_{transducer}$) was estimated by the square root of the frequency spectrum of the received echo signal. The response of the SPR sensor was estimated by $F_{SPR} = F_{signal}/F_{transducer}$, where F_{signal} is the spectrum of the acoustic pressure-encoded SPR signal. To ensure accuracy, the comparison was performed within the 3-dB receiving-only bandwidths of the transducers, which provide sufficient SNR. Strikingly, the SPR sensor showed an ultra-flat (fluctuation: ±0.7 dB) frequency response over the entire range of 0.68–126 MHz. The actual bandwidth might be even higher, although it could not be experimentally tested due to the finite (i.e., non-zero) duration of the impulse generated by the pulser-receiver.

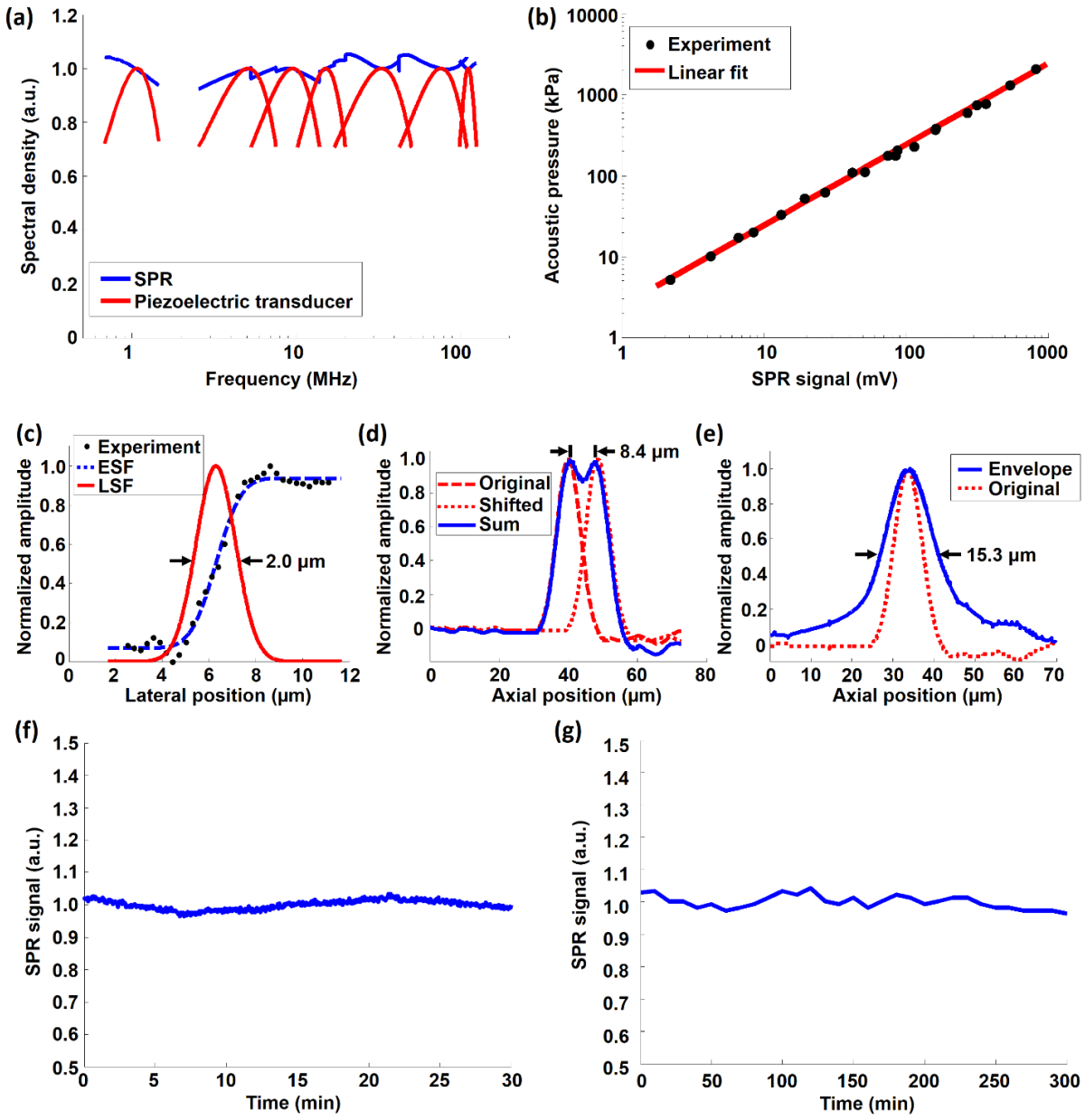

Fig. 2.4 Performance of the SPR-PAM. Comparison of the frequency responses of the SPR-based acoustic sensor and piezoelectric transducers. (b) Amplitude response of the SPR sensor to different acoustic pressures. The result shows linear response of the SPR sensor (R^2 = 0.99) to acoustic pressure over the range of 5.2 kPa–2.1 MPa. (c) Lateral resolution of the SPR-PAM quantified using the edge spread function. The measured result is 2.0 μm. ESF, error spread function; PSF, point spread function. (d) Axial resolution of the SPR-PAM quantified using the shift-and-sum method [54]. The result is quantified as 8.4 μm. (e) Axial resolution of the SPR-PAM quantified by the FWHM value of the A-line signal envelope. The result is 15.3 μm. (f) Short-term stability, the relative standard deviation is 1.3%. (g) Long-term stability, the relative standard deviation is 2.1%.

The linearity of the SPR response to acoustic pressure was examined using a focused transducer (V309, Olympus) driven by the pulser-receiver at different levels of impulsive energy. Prior to the SPR experiment, the amplitudes of the emitted acoustic pressures were calibrated by a commercial hydrophone (HGL-0085, Onda). Our result shows an excellent linear response of the SPR sensor ($R^2 = 0.99$) to acoustic pressure over the range of 5.2 kPa–2.1 MPa [Fig. 2.4(b)]. It is worth noting that we did not further push the upper boundary to avoid possible damage to the hydrophone. By extrapolating the linear range down to the noise level, we estimated the noise-equivalent pressure of our SPR sensor to be 3.3 kPa.

To quantify the lateral resolution, we first measured the edge spread function (ESF) of the SPR-PAM at 532 nm using a sharp metal edge generated by photolithography [Fig. 2.4(c)]. By taking the first-order derivative of the error function-fitted ESF, we derived the line spread function (LSF). The lateral resolution—defined as the full-width at half-maximum (FWHM) value of the LSF—was quantified to be 2.0 μm, which agrees with the diffraction-limited theoretical value (1.9 μm).

The axial resolution was measured using a 200-nm gold film. Since the thickness of the film is much smaller than the acoustic wavelength, it can be considered as a planar target. As shown in Fig. 2.4(d), the axial resolution was characterized using the shift-and-sum method. Briefly, the depth-resolved A-line signal of the gold film acquired by the SPR-PAM was gradually shifted away from its original position, until the sum of the two signals showed a bimodal shape and the dip between the two peaks dropped below 90%. The axial resolution, defined as the distance between the two peaks, was quantified to be 8.4 μm. Note that the Hilbert transform is often used to extract the envelope of the bipolar A-line signal for 3D rendering, which inevitably broadens the temporal profile of the signal [Fig. 2.4(e)]. As a consequence, the axial resolution—defined as

the FWHM of the signal envelope in this case—degrades to 15.3 μm. A similar discrepancy in the axial resolutions measured by the two different approaches has been reported before.

The stability of our SPR-PAM was also examined both short-termly and long-termly. A black tape as the absorption target was placed on the glass slide and excited by laser to generate acoustic wave. For short-term measurement, photoacoustic signal detected by the SPR sensor was collected by the waveform digitizer for ~30 minutes and the peak-to-peak value was extracted to quantify the signal amplitude. The signal fluctuation quantified by its standard deviation value was 1.3% [Fig. 2.4(f)]. For long-term measurement, the peak-to-peak value of photoacoustic signal was measured from the oscilloscope every 10 minutes for 5 hours. The signal fluctuation was 2.1% [Fig. 2.4(g)]. This superior stability of SPR-PAM ensures it can be practically applied for imaging.

As an initial demonstration of its capability of high-resolution volumetric imaging of biological samples, we performed SPR-PAM of a fixed melanoma cell with 100-nJ pulse energy and 0.83-μm step size. Murine melanoma B16 cells (ATCC) were grown in the tissue culture flasks in Dulbecco's Modified Eagle Medium (DMEM) media supplemented with penicillin-streptomycin and pyruvate. For imaging purposes, cells were subjected to trypsin/ ethylenediaminetetraacetic acid (EDTA) and deposited on the glass slide. After deposition, cells were grown until ~30% confluency, and fixed with 10% neutral formalin for 10 min. Fig. 2.5(a) and Fig. 2.5(b) are the maximum amplitude projected two-dimensional (2D) image and 3D rendering, respectively. To examine the spatial resolution, a single melanosome in the SPR-PAM image was analyzed. Since the diameter of melanosome (<500 nm) is much smaller than both the optical focal diameter and the acoustic wavelength, it can be considered as a point target. Thus, the volumetric profile of the melanosome reflects the point spread functions of our SPR-PAM along all three dimensions. Laterally, the Gaussian-fitted profile of the melanosome has a FWHM value of 2.2 μm along the

x direction [Fig. 2.5(c)] and 2.1 μm along the Y direction [Fig. 2.5(d)], both of which well correspond to the 2.0-μm lateral resolution of the system. Axially [Fig. 2.5(e)], the Gaussian-fitted envelope profile of the A-line melanosome signal has a FWHM value of 16.6 μm, which is slightly worse than the 15.3-μm axial resolution quantified using the 200-nm gold film.

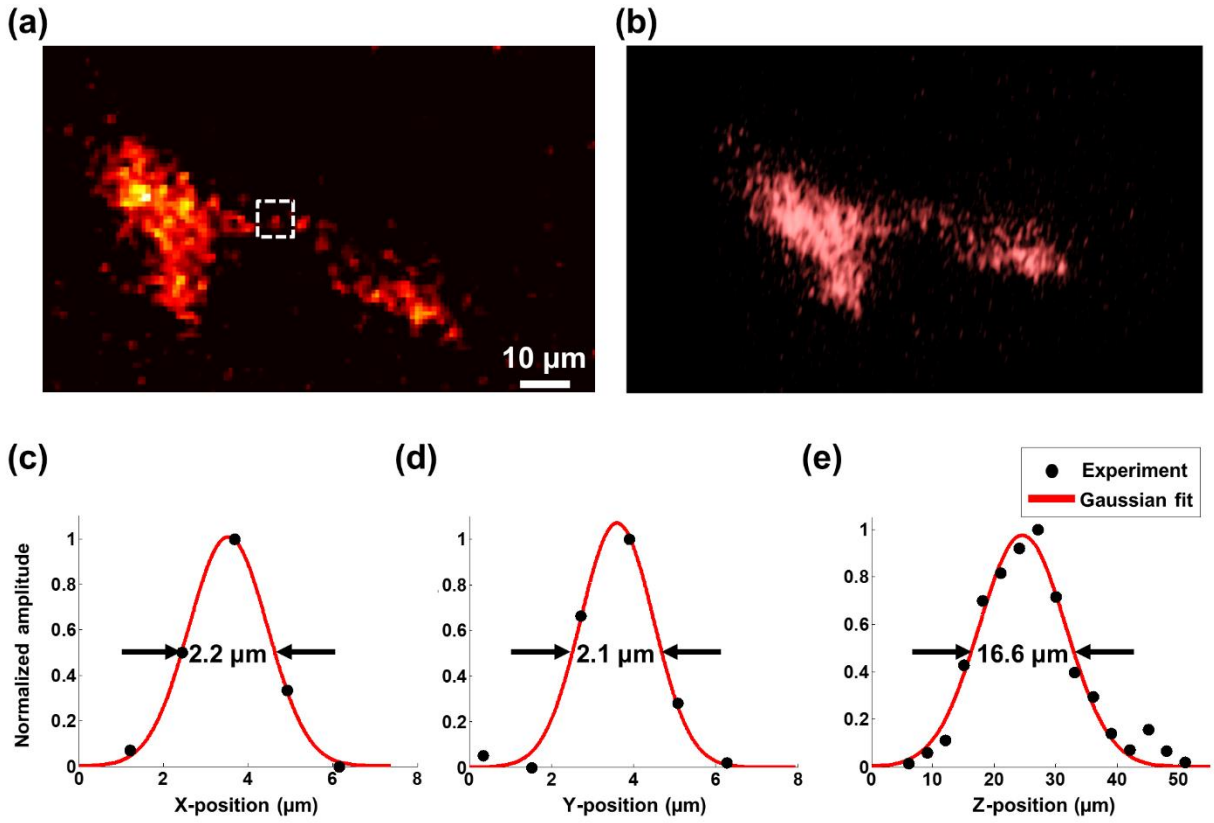

Fig. 2.5 High-resolution volumetric SPR-PAM of a fixed melanoma cell. (a) Maximum amplitude projected image. (b) Screenshot of the 3D rendering. (c–e) are the Gaussian-fitted profiles of a melanosome along the X, Y and Z direction, respectively. The FWHM of Gaussian-fitted profile along X, Y and Z direction are 2.2 μm, 2.1 μm and 16.6 μm respectively.

2.4 Summary

In summary, we have implemented an all-optical PAM based on plasmonic detection of ultrasound. The ultra-flat frequency response (±0.7 dB) from near-DC to over a hundred MHz

refines the axial resolution of PAM down to 8.4 μm. The excellent linear response (R^2 = 0.99) to acoustic pressures from 5.2 kPa to 2.1 MPa lays the potential of the SPR-PAM for quantitative imaging.

It is worth pointing out that the flat frequency response of the SPR sensor characterized by using pulse-echo indicates that its 3-dB bandwidth is higher. More accurate assessment of this parameter requires eliminating the bandwidth limiting factors in our current system, including the 3-dB bandwidth of the photodetector (200 MHz), the full-power bandwidth of the waveform digitizer (250 MHz), and the laser pulse duration (4.4 ns) that limits the bandwidth of the generated photoacoustic wave.

There is considerable opportunity for improving the sensitivity of our SPR-PAM. Replacing water with a liquid that has a higher acousto-optic coupling coefficient will enhance the pressure-induced change in the refractive index. For example, the acousto-optic coupling coefficient of ethanol is 3-fold higher than that of water can potentially improve the sensitivity of SPR sensor by 3-fold. Adopting the long-range SPR [55] or phase-detection method previously developed for other sensing applications and utilizing a probe laser with lower intensity fluctuation may boost the sensitivity by as much as an order of magnitude. Replacing the photodetector with a CCD camera can both improve the sensitivity and measure the time evolution of acoustic field at the gold-water interface thus realizing photoacoustic tomography [56].

Chapter 3

Isotropic-resolution Photoacoustic Microscopy with Multi-angle Illumination

3.1 Introduction

In chapter 2, we introduced the implementation of an SPR-PAM to improve axial resolution. There are several factors that limit its application in practical physiological studies. First, the SPR sensor has relatively poor sensitivity. The noise equivalent pressure is estimated as 3.3 kPa which is more than one order of magnitude worse than piezo-transducer. Second, the SPR-PAM can only work in transmission mode which is not practically possible in many *in vivo* imaging situations. In this chapter, we will introduce MAI-PAM with isotropic resolution that overcomes the above mentioned limitations.

Multi-view deconvolution is an emerging approach used in light-sheet microscopy to image the target from multiple view angles for improved spatial resolution and contrast. Lately, this concept was introduced to the field of PAM. Multi-view deconvolution of the images acquired by conventional PAM at different

view angles has led to improved axial resolution. Although encouraging, this method requires the rotation of imaging target and thus is not applicable to most animal studies *in vivo*, such as microvascular imaging in live rodents.

In this chapter, we propose to achieve the multi-view image acquisition by using multi-angle illumination, which circumvents animal rotation. According to the previous multi-view study using conventional PAM and animal rotation [57], Balancing deconvolution accuracy and system complexity, we choose a configuration of three illumination beams with incident angles of 45°, 90° (i.e., perpendicular to the imaging target) and 135° in X-Z plane, respectively. In this design, PAM images from all three-view angles can be acquired simultaneously for deconvolution-based image reconstruction, without the rotation of imaging target.

3.2 Principle and Simulation

The principle of MAI-PAM is similar to that of multi-view PAM. As shown in Fig. 3.1(a,c,e) [57], in conventional PAM, when two absorbers are close to each other along Z-axis, due to the poor axial resolution, conventional PAM cannot distinguish them. However, as shown in Fig. 3.1(b,d), by rotating the sample by 90 degrees, these two absorbers can be effectively distinguished due to the high lateral resolution. Thus, as shown in Fig. 3.1(f), combining the information from both images by using multi-view deconvolution algorithm, we can achieve isotropic resolution PA imaging.

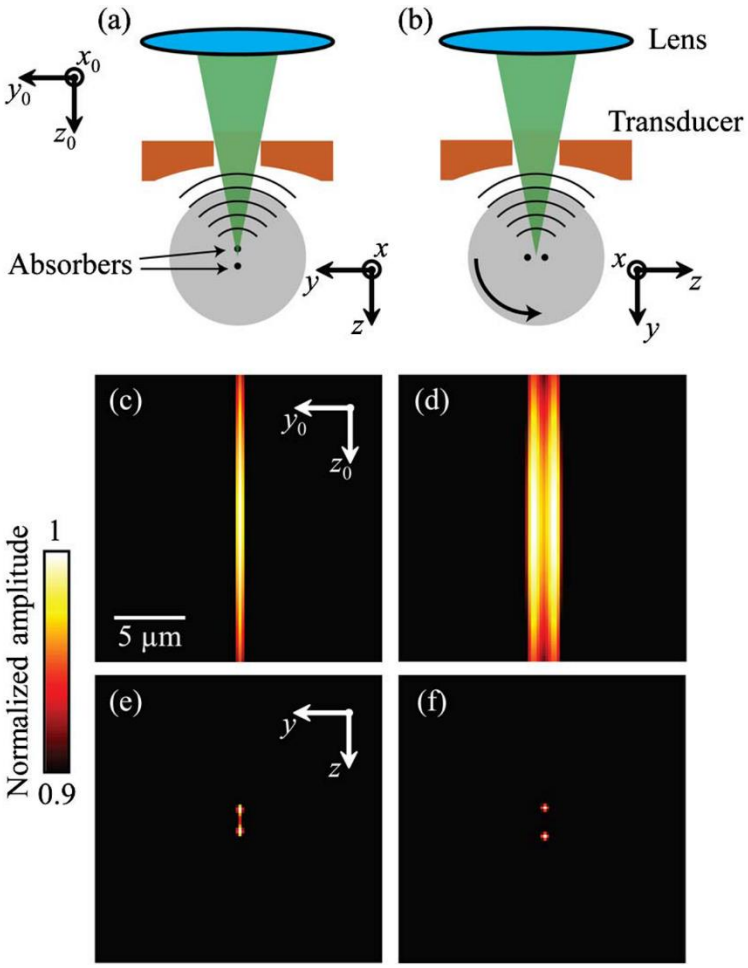

Fig. 3.1 Principle of multi-view PAM. (a, c, e) In conventional PAM, when two absorbers are close to each other along Z-axis, they are not distinguishable due to the poor axial resolution. (b, d) By rotating the sample by 90°, they are distinguishable due to the high later resolution. (f) Combing both images of (c) and (d) by using multi-view deconvolution algorithm, the two absorbers can be effectively distinguished and the system can achieve isotropic spatial resolution.

Prior to the real experiment, we firstly examine the relationship between axial resolution and number of views. As shown in Fig. 3.2(a) [57], theoretically, a minimal number of two views is sufficient to improve the resolution isotropy to 0.8. However, the simulation results shown in Fig. 3.2(b) clearly show that the dual-view configuration is associated with excessive artefacts induced by the deconvolution algorithm. Such artefacts can be reduced by increasing the number of views. Balancing deconvolution accuracy and system complexity, we choose a configuration of three illumination beams with incident angles of 45°, 90°

(i.e., perpendicular to the imaging target) and 135° in X-Z plane, respectively. As shown in Fig. 3.2(b), with triple-view configuration, the reconstructed image matches the ground truth and there is no observable artefacts.

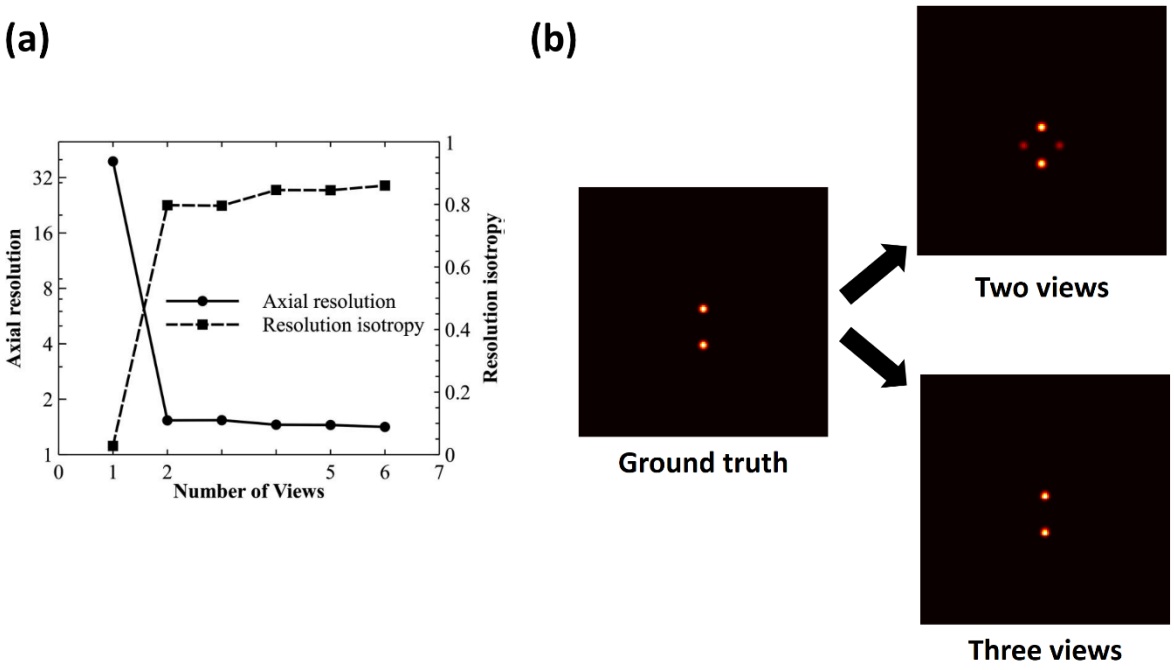

Fig. 3.2 Relationship between axial resolution and number of views. (a) Theoretical relationship between axial resolution and number of views. (b) Numerical simulation of applying multi-view deconvolution algorithm to reconstruct the ground truth with two and three views respectively. In the two-view result, the artefact induced by deconvolution algorithm can be observed. In the three-view result, there is no artefact.

After determining the number of views, a numerical simulation has been performed to further demonstrate that our scheme can improve axial resolution. In the simulation, 3.6-μm-diameter absorbers are randomly distributed in the X-Z plane. Incident beams with focal diameters of 3-μm and incident angles of 45°, 90° and 135° are launched onto the absorbers to generate photoacoustic signals. An ultrasonic transducer with a central frequency of 30 MHz and a 6-dB bandwidth of 70% is used. The transducer is

coaxially aligned with the 90°-incident beam. The foci of all three optical beams and the ultrasonic transducer are overlapped for maximum sensitivity. An iteration-based algorithm for multi-view deconvolution has been previously developed for light-sheet microscopy [58]. According to this algorithm, the equations for three-view imaging at each iteration are

$$u_{45} = \frac{I_{45}}{\hat{f}^{(r)} * g_{45}} * g'_{45} \tag{1}$$

$$u_{90} = \frac{I_{90}}{\hat{f}^{(r)} * g_{90}} * g'_{90} \tag{2}$$

$$u_{135} = \frac{I_{135}}{\hat{f}^{(r)} * g_{135}} * g'_{135} \tag{3}$$

$$\hat{f}^{(r+1)} = \hat{f}^{(r)} \cdot u_{45} \cdot u_{90} \cdot u_{135} \tag{4}$$

where u_θ denotes the term associated with the illumination from angle θ, I_θ represents the PAM measurement at angle θ, g_θ represents the point spread function (PSF) of PAM with the incident angle of θ, g'_θ represents the flipped PSF at angle θ (i.e., $g'_\theta(x,y) = g_\theta(-x,-y)$), and $\hat{f}^{(r)}$ is the estimated object function at iteration r. The PSF of each view is determined by convolution of the optical and acoustic PSFs at that view angle. The detailed derivation and interpretation of the algorithm can be found in ref. [58]

This multi-view deconvolution algorithm is applied to reconstruct the PAM image of the aforementioned numerical phantom. According to the simulation result (Fig. 3.3), the PAM images of individual views, which are generated by convolution of the phantom and the corresponding PSFs show poor axial resolution and thus cannot distinguish two absorbers when they are close to each other along the Z-axis. However,

with the multi-view deconvolution, individual absorbers can be clearly resolved and the reconstructed image matches the ground truth. This numerical experiment suggests that the multi-angle-illumination PAM (MAI-PAM) is capable of improving the resolution isotropy.

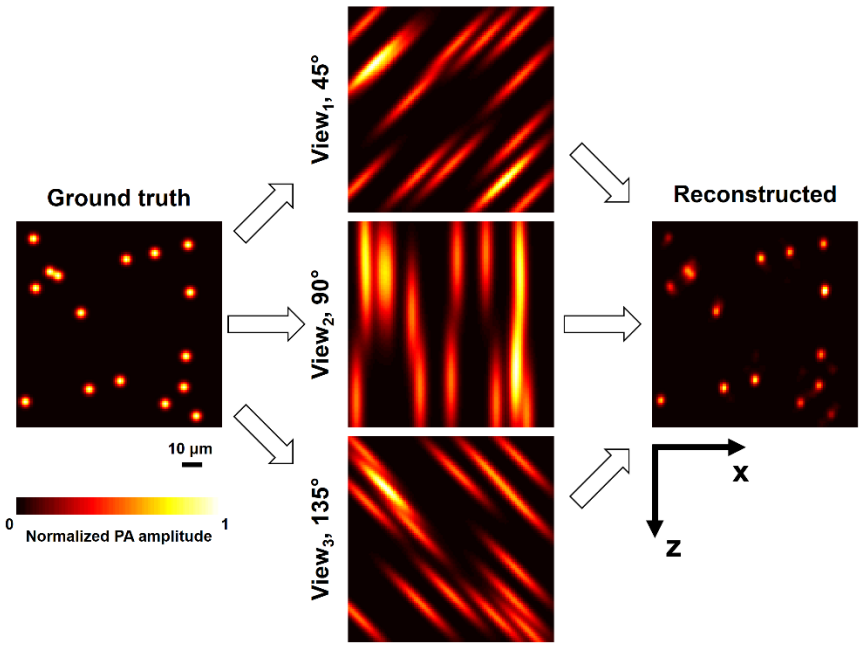

Fig. 3.3 Numerical simulation of MAI-PAM with three illumination angles. In the ground truth, 3.6-μm-diameter absorbers are randomly distributed in the X-Z plane, the image of view$_1$, view$_2$ and view$_3$ are generated via the convolution of their corresponding point spread function and ground truth, the reconstructed image is acquired by performing multi-view deconvolution algorithm on the three-view images. PA: photoacoustic.

Finally, to verify that the MAI-PAM is suitable for real-world applications, a numerical simulation is performed to examine the influence of SNR and PSF estimation error on reconstructed image respectively. In the real-world application, the acquired image are always noisy, thus we firstly examine the image reconstruction under different SNR. As shown in Fig. 3.4(a), when the SNR of each view is 5:1, the reconstructed image still matches the ground truth, however, when the SNR achieves 2:1, severe artefacts can be observed in the reconstructed image.

These results indicate that high SNR must be guaranteed in multi-view deconvolution. Also, due to tissue scattering, there will always be an estimation error between the physical PSF and theoretical PSF that we use in the multi-view deconvolution. To examine this relationship, we simulate the image reconstruction under different w_{real}/w_{deconv} values where w_{real} is the physical beam waist radius and w_{deconv} is the estimated beam waist radius that is used to calculate g_θ. As shown in Fig. 3.4(b), when the physical PSF becomes broader, the reconstructed image will also have poorer resolution, this indicates that to achieve micron-level resolution, tight optical focus must be achieved.

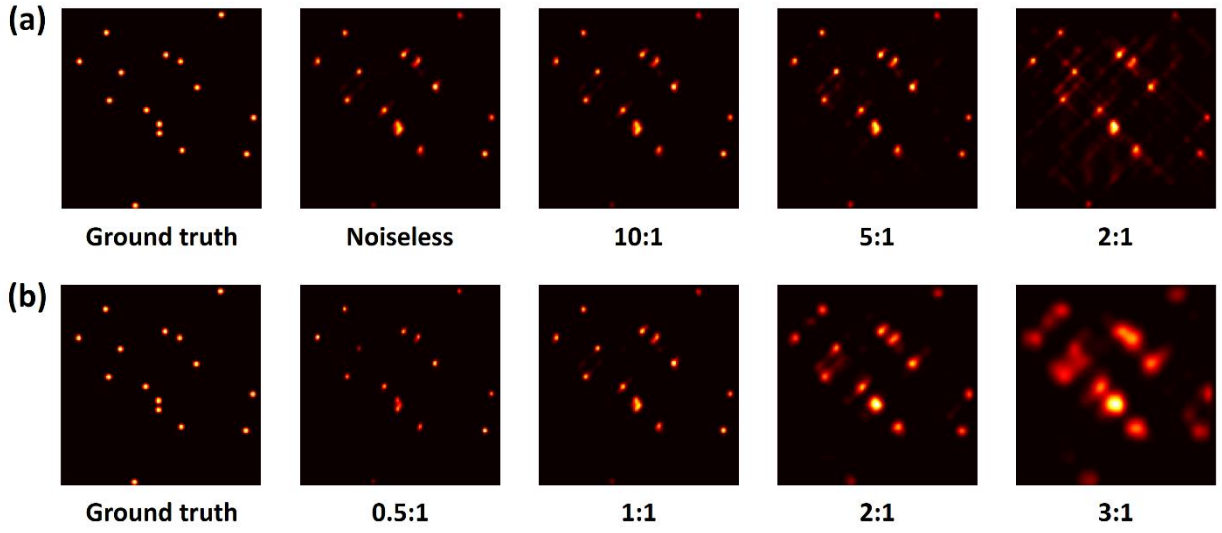

Fig. 3.4 Image reconstruction results under different SNR and PSF estimation error. (a) Image reconstructed by multi-view deconvolution algorithm when the SNR is infinity, 10:1, 5:1 and 2:1 respectively. (b) Image reconstructed by multi-view deconvolution algorithm under different w_{real}/w_{deconv} values where w_{real} is the physical beam waist radius and w_{deconv} is the estimated beam waist radius that is used to calculate g_θ.

3.3 Experimental Setup

With the validation of simulation, we have implemented MAI-PAM. As shown in Fig. 3.5(a), our MAI-PAM employs two 532-nm ns-pulsed lasers (GLPM-20-Y13, IPG Photonics) for PAM excitation. The output beam of $laser_1$ is coupled into a single-mode optical fiber (SMF_2; P1-460B-FC-2, Thorlabs) through a fiber collimator (CFC-11X-A, Thorlabs). In contrast, the output beam of $laser_2$ first passes through a half-wave plate (HWP; WPH05M-532, Thorlabs) and an electro-optical-modulator (EOM; 350-80, Conoptics). When a high voltage (260 V) is applied to the EOM, the polarization of the beam is rotated to the vertical direction by the EOM and HWP. Thus, the beam is reflected by a polarizing beam splitter (PBS; PBS121, Thorlabs) and coupled into a single-mode fiber (SMF_3) through a fiber collimator. When a low voltage (0 V) is applied to the EOM, the polarization of the beam remains horizontal. Thus, it passes through the PBS and is coupled into a single-mode fiber (SMF_1) through a collimator. During image acquisition, $laser_1$ and $laser_2$ are triggered alternately with a 100-μs interval, and the EOM voltage alternates between 0 and 260 V with an interval of 200 μs. With this configuration, the laser pulses are evenly allocated to the three fibers for multi-angle illumination. Also, the triggers for the waveform digitizer (DAQ, ATS9350, AlazarTech) are carefully designed, so that one A-line signal can be acquired from each laser pulse.

As shown in Fig. 3.5(b), in the scan head of MAI-PAM, the output beams from SMF_1 and SMF_3 are respectively collimated by a doublet (f = 25 mm, AC127-025-A, Thorlabs) and then focused into the imaging target via another identical doublet. A correction lens (LA1207-A, Thorlabs) is inserted into the optical path to compensate for the optical aberration at the air-water interface. Similarly, the output of SMF_2 is collimated by a doublet (f = 19 mm, AC127-019-A, Thorlabs) and then focused into the imaging target through a correction lens (LA1207-A, Thorlabs) and a doublet (f = 25 mm, AC127-025-A, Thorlabs). Following our numerical simulation, the incident angles of beams from SMF_1, SMF_2 and SMF_3 are aligned to be 45°, 90° and 135°, respectively, to generate images from different view angles. A ring-shaped

ultrasonic transducer (focal length, 5 mm; central frequency, 38 MHz; 6-dB bandwidth, 100%) is coaxially aligned with the 90° incident beam for ultrasonic detection. For optimal sensitivity, the focal spots of the three optical beams and the ultrasonic transducer are confocally aligned. For acoustic coupling, a homemade water tank is used to immerse the transducer and the correction lens. A thin layer of ultrasonic gel (Aquasonic CLEAR®, Parker Laboratories) is applied between the imaging target and the transparent polyethylene membrane at the bottom of the water tank. The entire imaging head is mounted on a three-axis motorized linear stage (PI miCos GmbH, PLS-85) for three-dimensional (3D) scan. PAM images from all three views are acquired simultaneously without the rotation of imaging target. The detected signals are acquired by DAQ and processed offline by MATLAB (R2014a, MathWorks). A field-programmable gate array (PCIe-7841R, National Instruments) is used to synchronize the lasers, EOM, 3D linear stage, and DAQ during image acquisition.

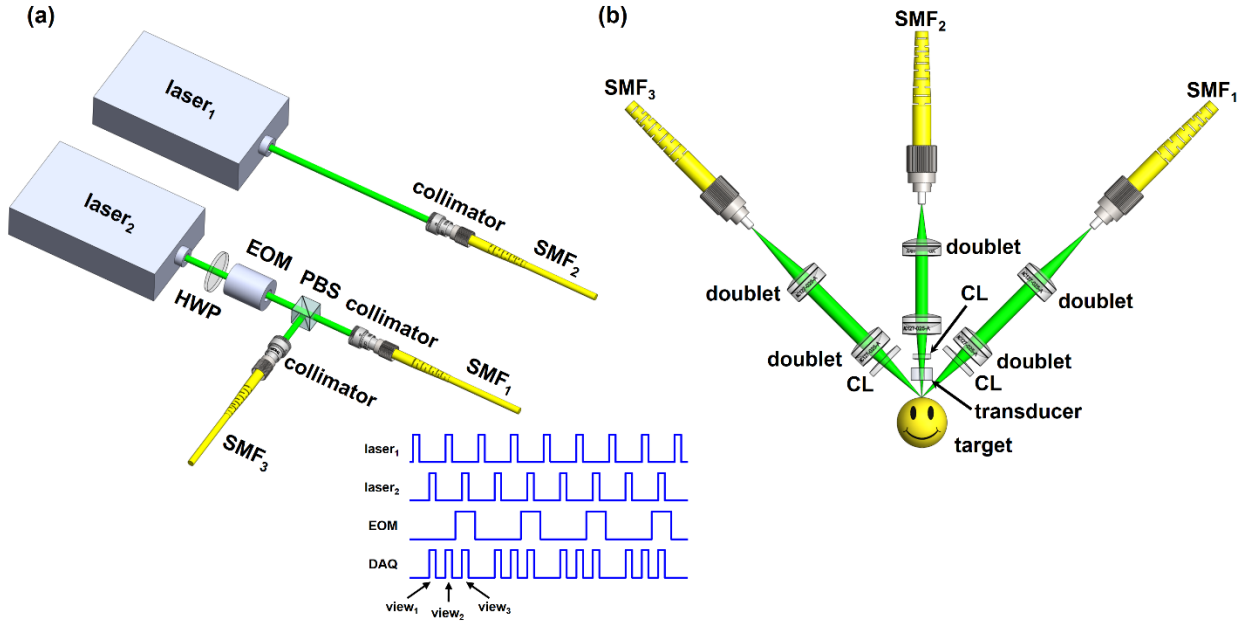

Fig. 3.5 Schematic of MAI-PAM. (a) Excitation sources and trigger scheme. HWP, half-wave plate; PBS, polarizing beam splitter; EOM, electro-optical modulator; SMF_1, SMF_2 and SMF_3, single-mode optical fibers. (b) Configuration of the imaging head. CL, correction lens.

3.4 Results

3.4.1 MAI-PAM of Carbon Fiber

A phantom study was performed to validate MAI-PAM. Specifically, Three 7-μm diameter carbon fibers (S-CF706-T700, CST) were carefully aligned and immobilized inside a piece of cured Polydimethylsiloxane. Then, MAI-PAM was applied to image these carbon fibers. At each scan position along the Y-axis, a two-dimensional (2D) scan was performed in the X-Z plane. At each scanning point, an A-line signal was obtained from each of the three views. Hilbert transform of individual A-lines was performed to recover the envelope of the signal, from which the peak-to-peak amplitude was extracted to form an X-Z cross-sectional image at each view. Ultimately, the multi-view deconvolution was performed to reconstruct an X-Z cross-sectional image with isotropic resolution [Fig. 3.7(a)]. For side-by-side comparison of the performance of MAI-PAM and conventional PAM, the Hilbert-transformed signals of the vertical view were used to form a single-view image provided by conventional PAM [Fig. 3.7(b)], in which the optical focal plane was indicated by the white dashed line. After the 2D raster scan in the X-Z plane, the linear stage moved to the next scan position along the Y-axis. Repeating this process for all X-Z planes and merging the reconstructed cross-sectional images resulted in a volumetric image (Fig. 3.6). It is apparent in both the X-Z images and the 3D movie that MAI-PAM significantly improved the axial resolution.

The improvement in resolution was characterized using quantitative analysis. As shown in Fig. 3.7(c) and Fig. 3.7(d), by applying Gaussian fitting, the FWHM values of carbon fibers imaged by MAI-PAM along both the X- and Z-axis were measured to be 7.5 μm and 7.9 μm, respectively. By contrast, the FWHM values along the X- and Z-axis were measured to be 8.6 μm and 39.0 μm in the corresponding image

acquired by conventional PAM. Since the measured results are the convolution of system PSF with the object profile, the FWHM of system PSF can be calculated by the equation $w_{system} = \sqrt{w_{measure}^2 - w_{object}^2}$ where w_{system} is the FWHM of system PSF, $w_{measure}$ is the measured FWHM that is acquired by quantifying the FWHM of the fitting curve to the experimental data and w_{object} is the width of imaging target. Taking the carbon fiber diameter of 7-μm into consideration, the lateral and axial resolution of MAI-PAM were estimated to be 2.7 μm and 3.7 μm, respectively. Both of which were finer than those of conventional PAM (5 μm laterally and 38.4 μm axially). This result shows that our MAI-PAM significantly improves the isotropy in PAM's resolution (from 0.13 in conventional PAM to 0.73). Moreover, with the help of the two side views, MAI-PAM improves the lateral resolution by a factor of ~2. Another advantage of MAI-PAM is that its spatial resolution remains unchanged across different depths. As shown in Fig. 3.7(e), the FWHM values of carbon fibers measured by MAI-PAM along the X- and Z-axis varied only by 1.3% and 5.0%, respectively, over a depth range of 330 μm. This result shows that MAI-PAM does not have the out-of-focus problem, which is a limiting factor in conventional PAM and needs to be addressed by sophisticated scanning strategies when imaging tissues within uneven surfaces [40].

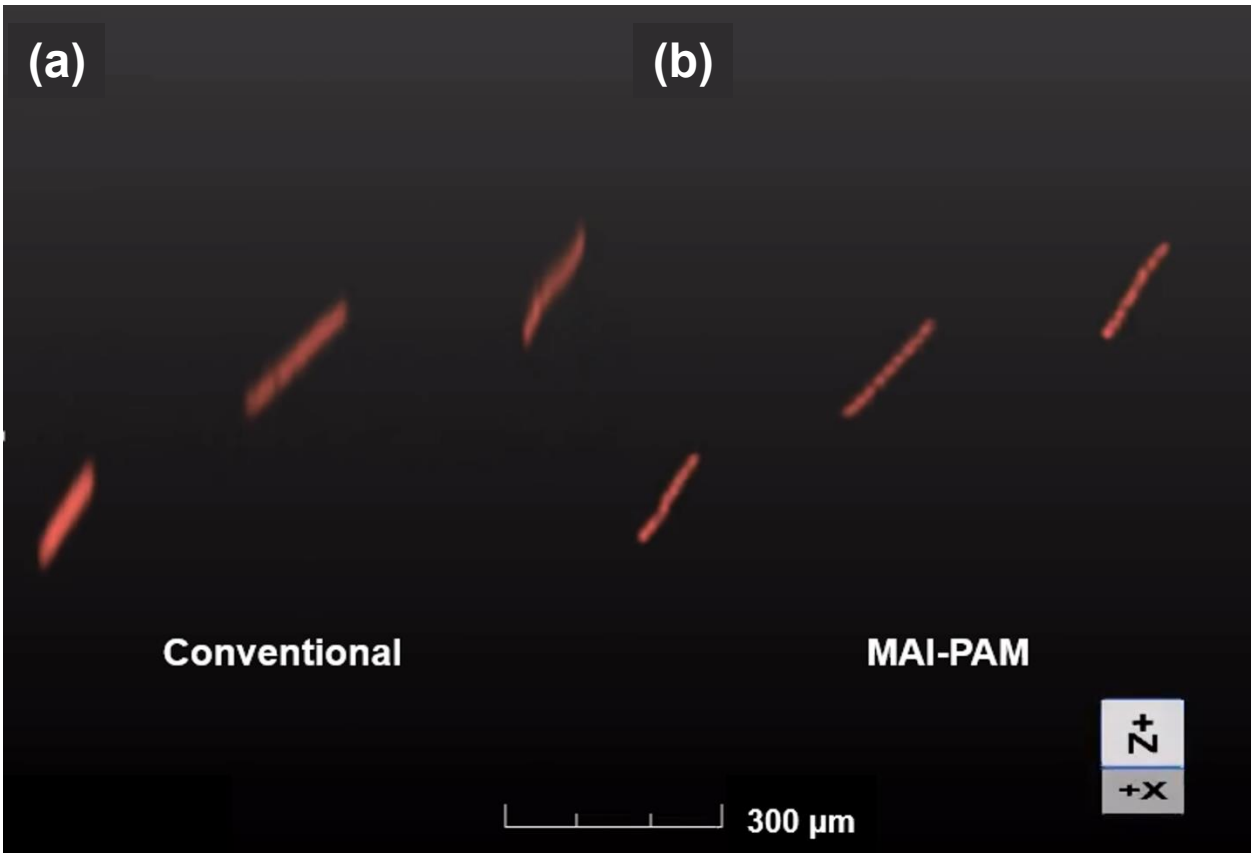

Fig. 3.6 Volume rendering of carbon fiber imaged by both MAI-PAM and conventional PAM. (a) Photoacoustic image acquired by conventional PAM. (b) Photoacoustic image acquired by MAI-PAM. According to the results, the image acquired by MAI-PAM show better resolution isotropy than image acquired by conventional PAM.

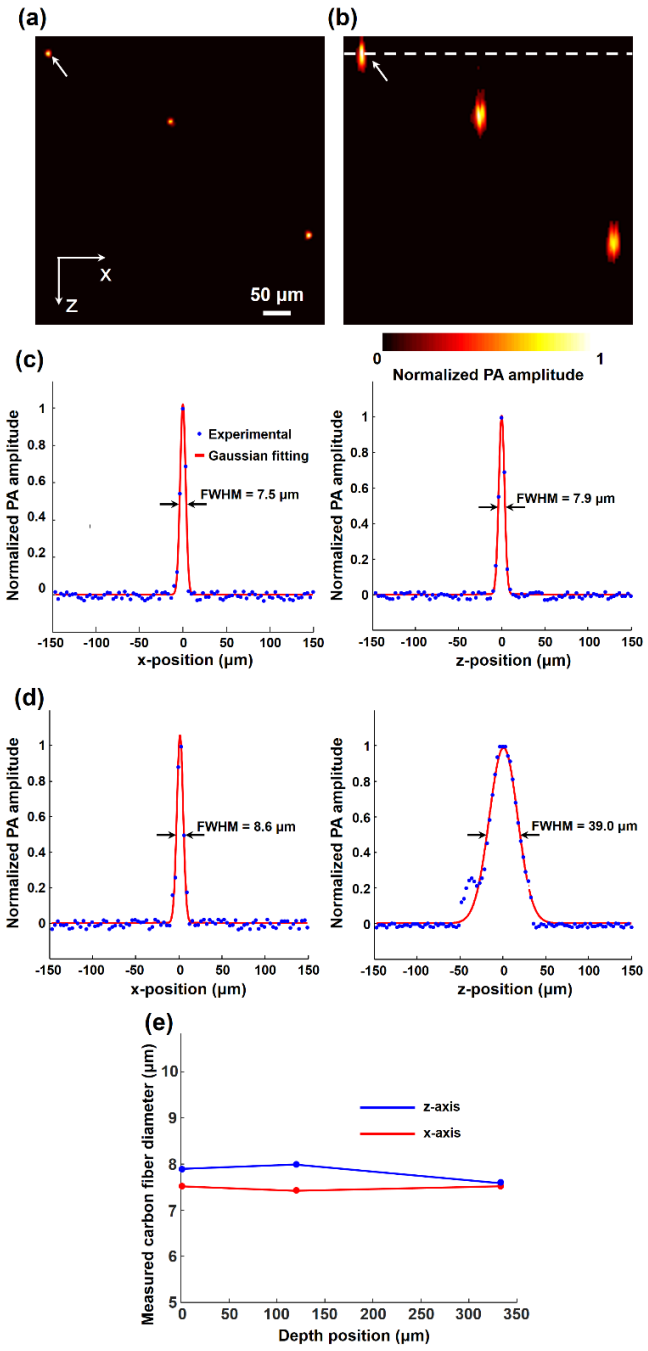

Fig. 3.7 Validation of MAI-PAM in phantom. (a-b), X-Z cross-sectional images of the carbon fibers acquired by MAI-PAM and conventional PAM, respectively. The white arrows indicate the carbon fiber analyzed in (c) and (d). The white dashed line represents the focal plane of conventional PAM. (c-d), quantitative comparison of the diameters of the carbon fiber imaged by MAI-PAM and conventional PAM along the X- and Z-axis. The measured FWHM of carbon fiber diameter along X-, Z-axis are 7.5, 7.9 μm respectively in MAI-PAM and 8.6, 39.0 μm respectively in conventional PAM. (e) FWHM values of the carbon fiber profile measured by MAI-PAM along the X and Z-axis and at different depths show constant value.

3.4.2 MAI-PAM of Mouse Ear *in vivo*

Further, the feasibility of MAI-PAM for *in vivo* applications was tested in the ear of a C57BL/6BrdCrHsd-Tyr c mouse (Envigo, 21 months old). Both MAI-PAM and conventional PAM of the ear were simultaneously performed over an image region of $300 \times 500 \times 200\ \mu m^3$. The image acquisition and reconstruction followed those used in the phantom test. The laser pulse energy of each view was 100 nJ respectively. Throughout the experiment, the mouse was maintained under general anesthesia with 1.5% vaporized isoflurane, and the body temperature was kept at 37°C by using a heating pad (SRFG-303/10, Omega) and a temperature controller (EW-89802-52, Cole-Parmer). All experimental procedures presented herein were carried out in conformity with the laboratory animal protocol approved by the Animal Care and Use Committee at the University of Virginia.

Compared to the X-Y maximum amplitude projection image acquired by MAI-PAM [Fig. 3.8(a)], the projection image acquired by conventional PAM over the same region [Fig. 3.8(b)] does not clearly show some of the microvessels (indicated by white arrows), due to the out-of-focus issue. More importantly, in the X-Z and Y-Z images acquired by conventional PAM, the vessel cross sections are elliptically shaped, which is due to the pronounced difference between the optically defined lateral resolution and acoustically defined axial resolution. Addressing this limitation with the additional views, MAI-PAM is able to remove the artefact and shows the true circular shape of the vessel cross section. As shown in Fig. 3.9, the improvement in resolution is further demonstrated by side-by-side comparison of the volumetric images acquired by MAI-PAM and conventional PAM.

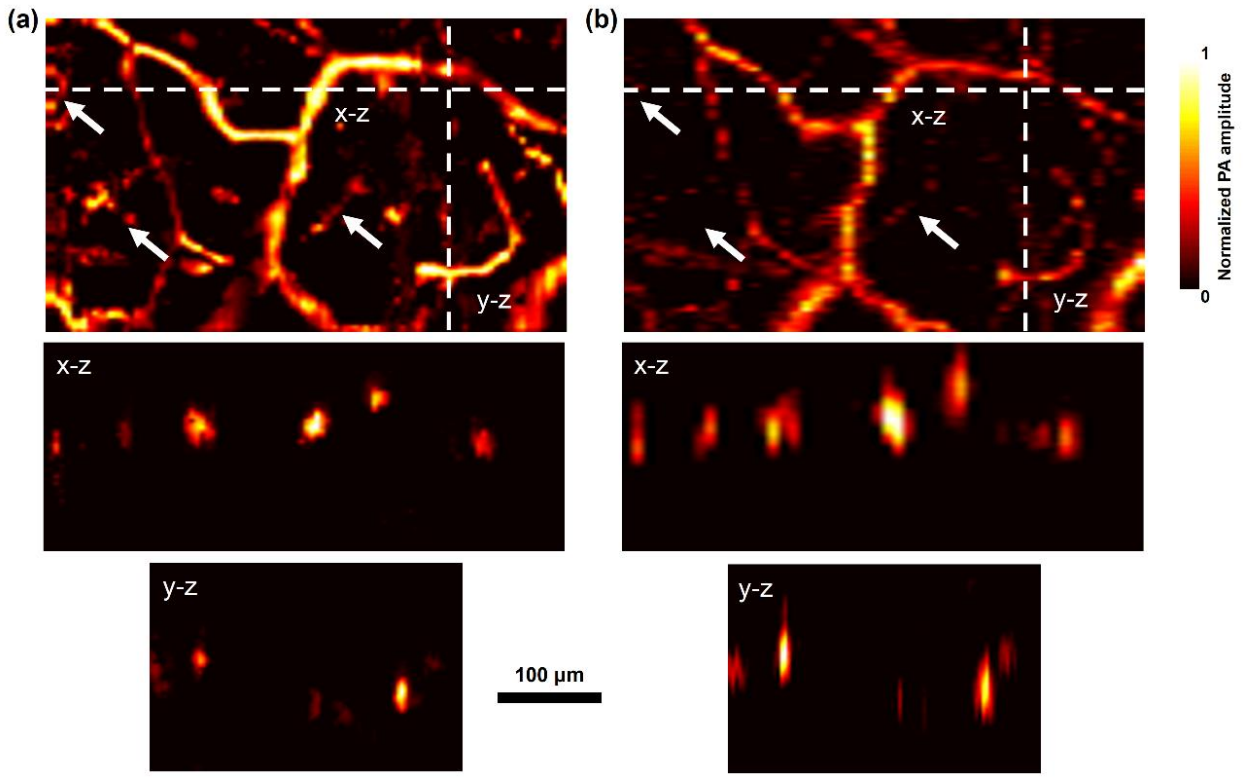

Fig. 3.8 Experimental results of *in vivo* MAI-PAM and conventional PAM of mouse ear. (a-b), X-Y maximum projection image, X-Z and Y-Z cross section image acquired by MAI-PAM and conventional PAM respectively. The projection image acquired by conventional PAM over the same region does not clearly show some of the microvessels (indicated by white arrows), due to the out-of-focus issue. In the X-Z and Y-Z images acquired by conventional PAM, the vessel cross sections are elliptically shaped, which is due to the pronounced difference between the optically defined lateral resolution and acoustically defined axial resolution. Addressing this limitation with the additional views, MAI-PAM is able to remove the artefact and shows the true circular shape of the vessel cross section.

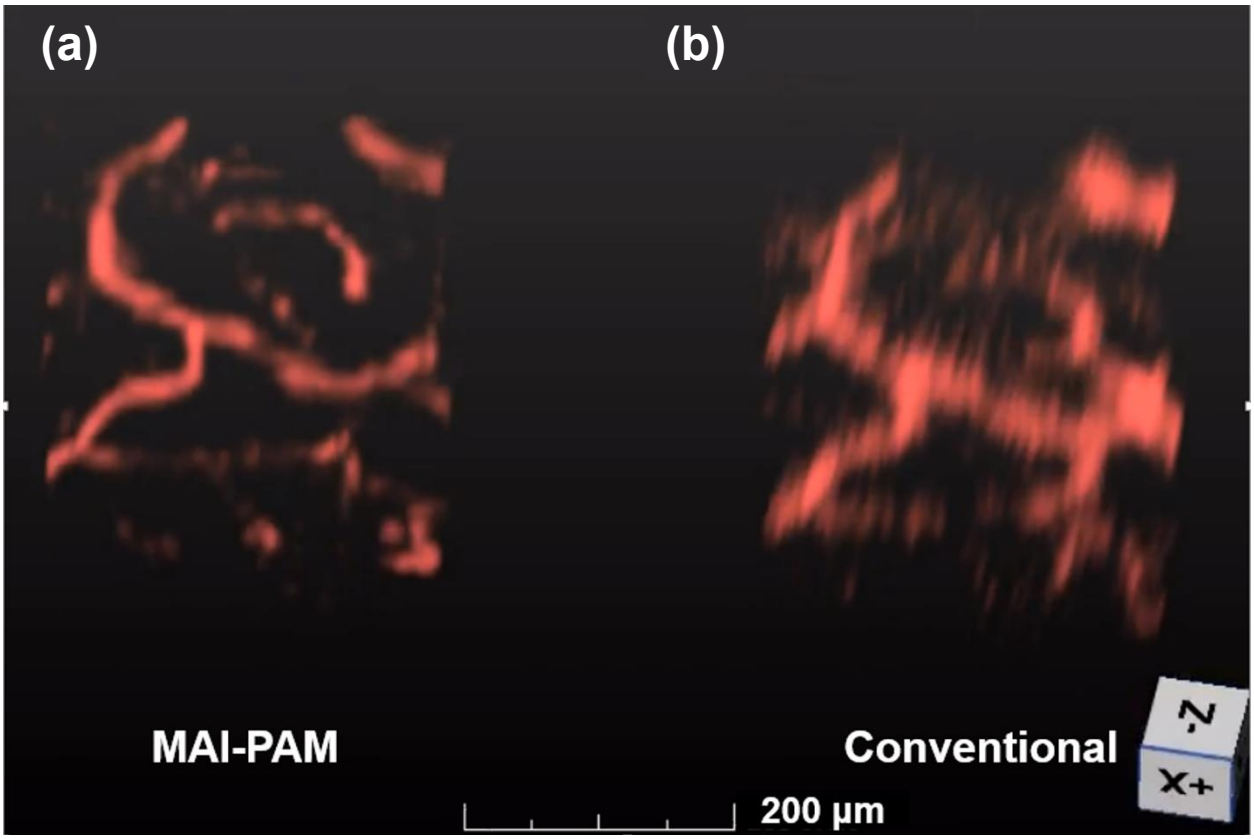

Fig. 3.9 Volume rendering of mouse ear vasculature imaged by MAI-PAM and conventional PAM. (a). 3D photoacoustic imaging acquired by MAI-PAM. (b) 3D photoacoustic imaging acquired by conventional PAM. The results clearly show that MAI-PAM have better resolution isotropy.

3.5 Summary

In summary, we have developed MAI-PAM for high-resolution photo-acoustic imaging with micron-level isotropic spatial resolution *in vivo*. By using three illumination beams with difference incident angles, this imaging system is capable of realizing multi-view image acquisition and reconstruction without the rotation of imaging target. We validated this technique both in phantom (Fig. 3.7) and *in vivo* (Fig. 3.8). The phantom study shows that MAI-PAM has achieved a 10-fold improvement on axial resolution over conventional PAM. The *in vivo* study further confirms the improvement in resolution isotropy over conventional PAM. Future work includes the improvement of imaging speed by applying optical-

mechanical hybrid scan [59] and implementation of functional measurements including blood perfusion, oxygenation and flow with our previously developed multi-parametric analysis [41].

Chapter 4

Multi-parametric Photoacoustic Microscopy of the Mouse Brain with 300-kHz A-line Rate

4.1 Introduction

Capable of providing label-free, comprehensive, and quantitative characterization of cerebral hemodynamics at the microscopic level, PAM has attracted increasing attention in neuroimaging [60]. A recent research focus is to combine the multiple PAM-measured hemodynamic parameters—including C_{Hb}, sO_2, and CBF—for quantifying the cerebral metabolic rate of oxygen ($CMRO_2$) at the microscopic level [9,61]. To this end, we have developed multi-parametric PAM, which enables simultaneous imaging of C_{Hb}, sO_2, and CBF at the same spatial scale [40]. However, the speed of multi-parametric PAM has been severely limited by the pulse repetition rate of the dual-wavelength photoacoustic excitation and the scanning mechanism. By employing two commercially available high-repetition single-wavelength lasers with distinct pulse durations (3 ns and 3 ps) and a customized water-immersible MEMS (microelectromechanical-system) scanning mirror, Yao *et al.* have markedly improved the speed of PAM and demonstrated functional imaging of the mouse brain with 100-kHz A-line rate [62]. Although encouraging, this technique is not applicable for microscopic imaging of $CMRO_2$ because CBF—unlike the other

two parameters—can only be measured at selected locations. Moreover, the pulse-duration-based measurement of sO_2 requires high laser pulse energy (>400 nJ) to induce transient saturation in the optical absorption of blood hemoglobin, exceeding the safety limit recommended by the American National Standards Institute.

In this chapter, we report on a new implementation of multi-parametric PAM with an unprecedented A-line rate of 300-kHz. This technique sticks to the established spectroscopic measurement of sO_2, which requires much lower pulse energy (<100 nJ) than the saturation-based approach. To allow for high-repetition dual-wavelength excitation, we have developed a 300-kHz laser capable of pulse-by-pulse switching between 532 and 558 nm. To boost the imaging speed while retaining the unique capability of simultaneously mapping C_{Hb}, sO_2, and CBF at the microscopic level, we have implemented optical-mechanical hybrid scan to acquire multiple cross-sectional scans (i.e., B-scans) in parallel. The performance of this new generation of multi-parametric PAM has been examined in phantoms and the mouse brain.

4.2 Materials and Methods

4.2.1 Experimental Setup

As shown in Fig. 4.1, the high-speed multi-parametric PAM utilizes an ytterbium-doped fiber laser (GLPM-10-Y13, IPG Photonics; wavelength: 532 nm; pulse repetition rate: tunable between 10–300 kHz; pulse duration: 1.25 ns). The laser beam passes through an electro-optical modulator (EOM; 350-80, Conoptics) and a half-wave plate (HWP; WPH05M-532, Thorlabs) before being expanded by a lens pair (LA1213-A and LA1608-A, Thorlabs). When a high voltage (260 V) is applied to the EOM, the polarization of the incident beam is rotated to the vertical direction by the

EOM and HWP. Thus, the expanded beam is reflected by a polarizing beam splitter (PBS; PBS121, Thorlabs) and then coupled through a microscope objective (M-10X, Newport) into a 5-meter-long polarization-maintaining single-mode fiber (PM-SMF; F-SPA, Newport) for stimulated Raman scattering-based wavelength conversion [63,64]. To maximize the conversion efficiency, the orientation of the PM-SMF is carefully adjusted to align its principal axis with the polarization of the incident light [65]. The output of the PM-SMF is collimated by a collimator (CFC-11X-A, Thorlabs) and purified by a bandpass filter (FB560-10, Thorlabs) to isolate the 558-nm component. When a low voltage (0 V) is applied to the EOM, the 532-nm beam is horizontally polarized after expansion and passes through the PBS without wavelength conversion. Thus, alternating the EOM voltage allows pulse-by-pulse switching of the laser wavelength. The unconverted 532-nm beam and the 558-nm Raman beam are combined via a dichroic mirror (FF538-FDi01, Semrock) and coupled into the imaging head through a 2-meter-long regular single-mode fiber (SMF; P1-460B-FC-2, Thorlabs), before which ~5% of the combined beam is picked off by a beam sampler (BSF10-A, Thorlabs) and monitored by a high-speed photodiode (FDS100, Thorlabs) to compensate for possible fluctuation in the laser energy. According to our test, the regular SMF with such a short length does not generate noticeable Raman shift to the optical wavelength. In the imaging head, the dual-wavelength beam is collimated by an achromatic doublet (AC127-019-A, Thorlabs), reflected by a two-axis galvanometer scanner (6215HSM40B, Cambridge Technology), and then focused into the object to be imaged by a second doublet (AC127-025-A, Thorlabs) through a correction lens (KPX561, Newport) and the central opening of a customized ring-shaped ultrasonic transducer (inner diameter: 2.0 mm; outer diameter: 4.4 mm; focal length: 5.0 mm; center frequency: 41 MHz; 6-dB bandwidth: 61%).

The imaging head is mounted on two motorized linear stages (PLS-85, PI miCos) for raster scan. A homemade water tank is used to immerse the transducer and the correction lens. A thin layer of ultrasound gel (Aquasonic CLEAR®, Parker Laboratories) is sandwiched between the object to be imaged and the transparent polyethylene membrane at the bottom of the water tank for acoustic coupling. A field-programmable gate array (PCIe-7842R, National Instruments) is used to synchronize the laser, EOM, galvanometer scanner, linear stages, and waveform digitizer (ATS9350, AlazarTech) during image acquisition.

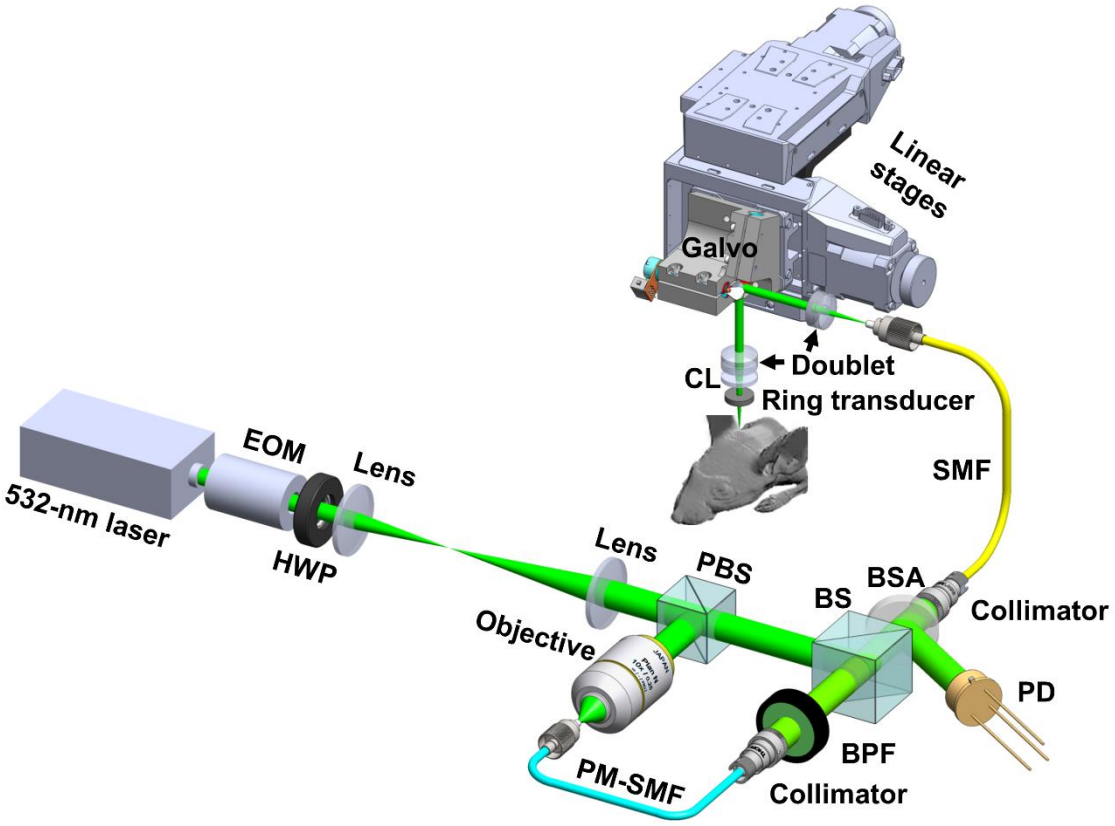

Fig. 4.1 Schematic of the high-speed multi-parametric PAM. EOM, electro-optical modulator; HWP, half-wave plate; PBS, polarizing beam splitter; PM-SMF, polarization-maintaining single-mode fiber; BPF, bandpass filter; DM, dichroic mirror; BSA, beam sampler; SMF, regular single-mode fiber; CL, correction lens.

4.2.2 Scanning Mechanism and Measurement Principle

Recent advances have led to dramatic improvements in the speed of PAM [62,66], but none of them permit CBF mapping at the microscopic level. The multi-parametric PAM provides a solution; however, the correlation-based CBF quantification limits its B-scan rate to ~1 mm/s. To boost the speed of PAM while maintaining the slow B-scan rate for the CBF measurement, we adopted the synchronized one-dimensional optical and two-dimensional (2D) mechanical hybrid scan [67]. As shown in Fig. 4.2(a), the galvanometer scanner steers the laser spot along the Y-axis within the acoustic focus of the transducer at a round-trip rate of 2.1 kHz as the linear stage mechanically translates the optical-acoustic dual foci along the X-axis at a constant speed of 0.88 mm/s, during which the laser output is switched between 532 and 558 nm at a 3.3-μs interval to produce dual-wavelength A-line pairs. The optical-mechanical hybrid scan forms a sinusoidal pattern, with 36 pixels acquired at each wavelength in a half-cycle. To assure an approximately constant pixel size along the Y-axis, for each wavelength, only the 20 pixels near the center of the optical scan are extracted for image reconstruction. Thus, 20 dual-wavelength B-scans can be simultaneously acquired, leading to a 20-fold increase in the imaging speed over our previously reported multi-parametric PAM, which is based on pure mechanical scanning [66].

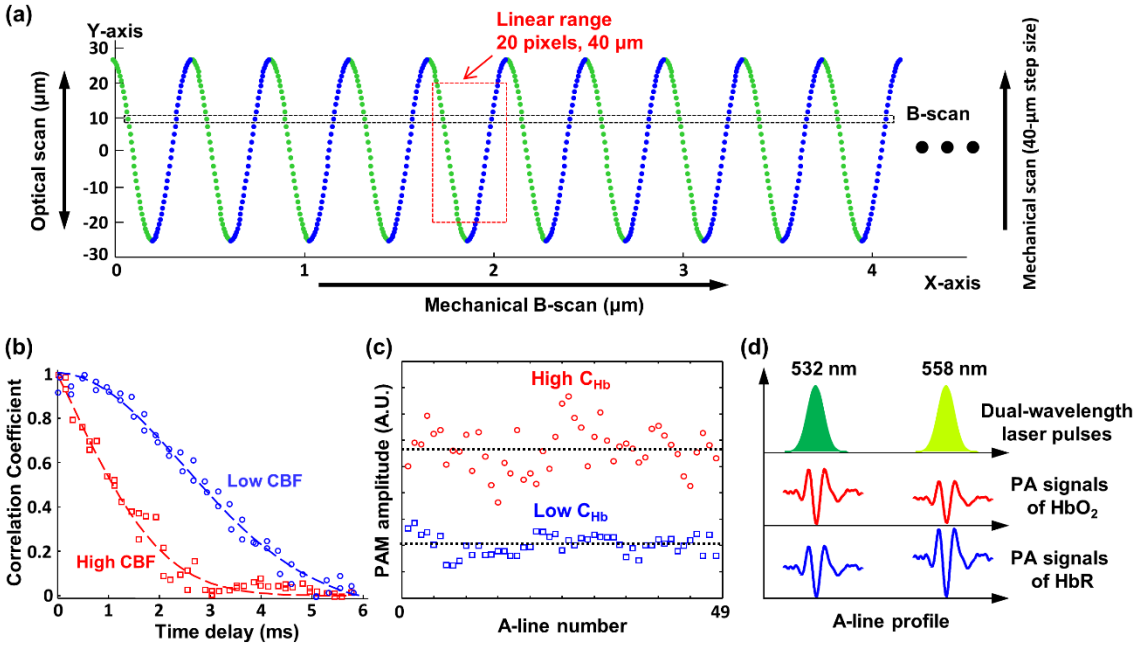

Fig. 4.2 Scanning mechanism and measurement principle. (a) Scanning scheme of the optical-mechanical hybrid scan. (b–d) Correlation, statistical, and spectral analysis of CBF, C_{Hb}, and sO_2, respectively. HbO_2, oxy-hemoglobin; HbR, deoxy-hemoglobin.

Simultaneous mapping of CBF, C_{Hb}, and sO_2 at the microscopic level is realized by correlation, statistical, and spectral analysis of individual B-scans [66]. Specifically, PAM is insensitive to sO_2 at 532 nm, a near-isosbestic point of hemoglobin. Fluctuations in the PAM signal acquired at this wavelength encode both the flow and Brownian motion of red blood cells (RBCs) [68]. The speed of CBF is quantified by the decorrelation rate of successively acquired A-lines. Theoretically, the correlation coefficient between two adjacent A-lines depends on their time interval [69]. The time dependence follows a second-order exponential decay, of which the decay constant is linearly proportional to the blood flow speed. As shown in Fig. 4.2(b), in plane CBF can be quantified by fitting the experimentally measured decorrelation curve with the theoretical model. The faster the decay, the higher the speed. Given the 2.1-kHz round-trip rate of the optical scan and the 0.88-

mm/s speed of the mechanical scan, 49 A-lines can be acquired when the linear stage travels 10 μm along the B-scan direction. The decorrelation curve is obtained by calculating the correlation coefficients between the central A-line and each of the 48 preceding and subsequent A-lines and the corresponding time delays. This correlation analysis allows CBF quantification at a spatial scale comparable to the average diameter of capillaries. Note that the measured speed is a vector summation of the speed of the linear stage and that of the CBF. The true CBF speed can be derived using the bi-directional scan as $\sqrt{\frac{1}{2}(v_f^2 + v_b^2 - 2v_m^2)}$, in which v_f and v_b are respectively the flow speeds measured by the forward and backward scan and v_m is the B-scan speed. [41] Furthermore, the difference between v_f and v_b reveals the direction of the flow. [70] In parallel, C_{Hb} can be derived in the absolute value by analyzing the Brownian motion-induced statistical fluctuation in the amplitudes of the same 49 A-lines, which is known to depend on the number of RBCs within the detection volume of PAM but not on the flow speed. As shown in Fig. 4.2(c), the higher the C_{Hb}, the larger the A-line amplitude and the higher the fluctuation. By comparing the readouts at both wavelengths (532 and 558 nm), sO_2 can be simultaneously quantified. As shown in Fig. 4.2(d), the absorption coefficients of oxy- and deoxy-hemoglobin are nearly identical at 532 nm but distinct at 558 nm. Thus, sO_2 can be estimated using spectral decomposition [22].

4.3 Animal Preparation

A male CD1 mouse (17 weeks old) was used for the *in vivo* study. For optimal imaging quality, the mouse skull above the right somatosensory cortex was thinned to ~100 μm prior to the PAM experiment, forming a circular imaging window with a diameter of ~3 mm. Throughout the PAM

experiment, the mouse was maintained under anesthesia with 1.0–1.5% isoflurane and the body temperature was kept at 37 °C using a temperature-controlled heating pad (EW-89802-52, Cole-Parmer; SRFG-303/10, Omega). All experimental procedures were carried out in conformity with the laboratory animal protocol approved by the Animal Care and Use Committee at the University of Virginia.

4.4 Results

4.4.1 Stability of the 558-nm Output

In stimulated Raman scattering, the Stokes light has a nonlinear dependence on the pump. Thus, small fluctuations in the 532-nm pump can be amplified when it is Raman-shifted. To check the stability of the 558-nm output, we continuously monitored the pulse energy for 660 seconds and the average power for 120 minutes using the high-speed photodiode and a power meter (S120C, Thorlabs), respectively. Prior to the monitoring, the coupling efficiency of the 532-nm incident beam to the PM-SMF was maximized and the incident pulse energy was set to 1 μJ, which led to a maximal 558-nm output of 220 nJ. The fluctuation of the room temperature was controlled within 1 °C to avoid possible disturbance to the 532-nm laser and the PM-SMF. As shown in Fig. 4.3, the relative standard deviation of the Raman pulse energy and power were measured to be 0.76% and 1.42%, respectively. Such small fluctuation could be easily compensated for by the high-speed photodiode monitoring during *in vivo* experiments.

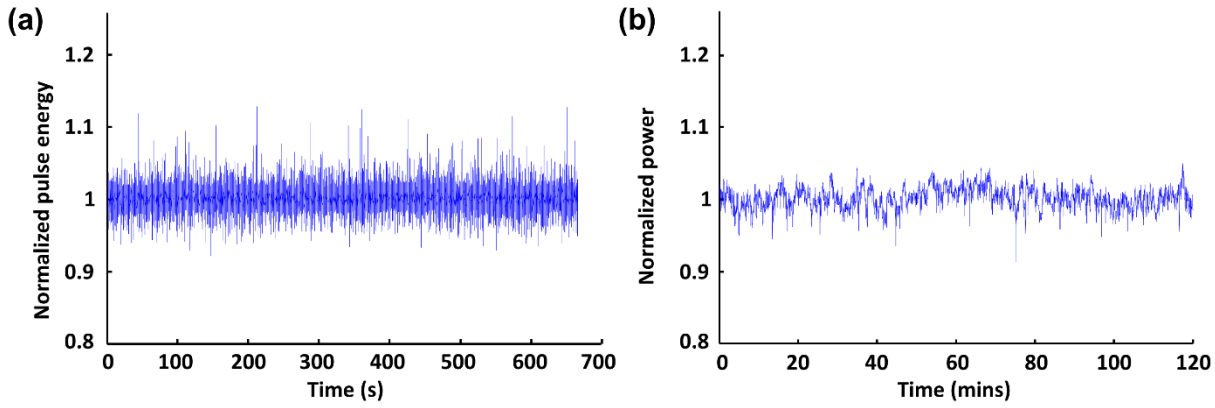

Fig. 4.3 Stability of the 558-nm Stokes output. (a) Short-term monitoring using high-speed photodiode. The relative standard deviation is 0.76%, (b) Long-term monitoring using power meter. The relative standard deviation is 1.42%.

4.4.2 Optical Resolution and Acoustic Focal Zone

The optically defined lateral resolution of the multi-parametric PAM was examined by imaging a resolution target (R1DS1P, Thorlabs). As shown in Fig. 4.4(a), the 6th element of Group 7 was clearly resolved. By fitting the experimentally measured modulation transfer function (MTF) to the theoretical MTF of a perfect optical system [71], we estimated the cutoff spatial frequency to be 259.7 line pair/mm, which corresponded to a lateral resolution of 3.9 μm.

For the optical-mechanical hybrid scan, the optical scanning must be confined within the focal zone of the ultrasonic transducer to ensure sufficient signal-to-noise ratio. The acoustic focus in the transverse plane was experimentally characterized by 2D optical scanning of a homogeneous black tape over an area of 65 μm by 65 μm. As shown in Fig. 4.4(b), the circular region with high photoacoustic amplitudes corresponded to the acoustic focal zone. Gaussian fitting of the cross-sectional profiles [dashed lines in Fig. 4.4(b)] revealed the acoustic focal diameters along the X and Y-axis to be 45 μm and 39 μm, respectively [Fig. 4.4(c)]. Thus, the voltage applied to the galvanometer scanner was carefully adjusted to spread the 20 pixels over the 40-μm range of

optical scanning. It is worth noting that the nonuniform detection sensitivity within the 40-μm acoustic focal zone, as shown in Fig. 4.4(b, c), was mathematically compensated for before the quantification of C_{Hb}, sO_2, and CBF.

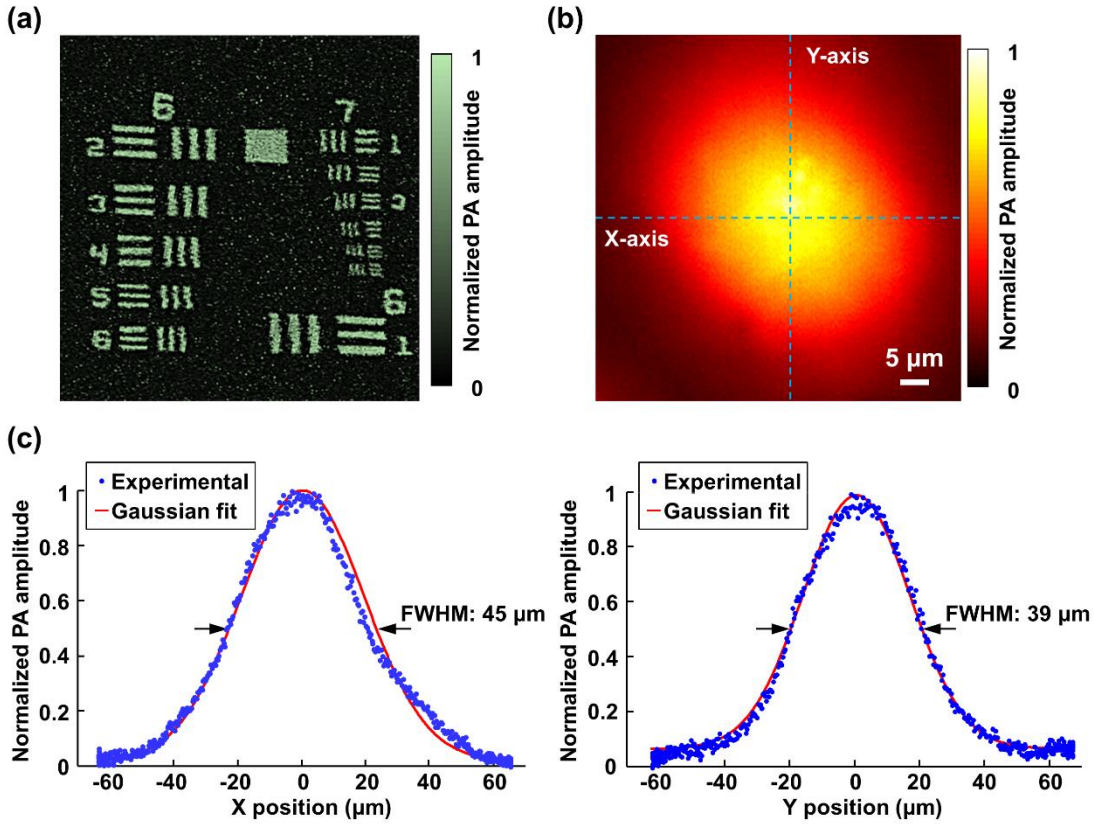

Fig. 4.4 Optical resolution and acoustic focal zone. (a) Optically defined lateral resolution quantified using a resolution target. The lateral resolution is estimated as 3.9 μm. (b) Acoustic focal zone along the lateral direction delineated by 2D optical scanning of a black tape. (c) Acoustic focal diameters along the X and Y-axis quantified by the full-width at half-maximum (FWHM) values of the Gaussian-fitted cross-sectional profiles. The transducer focal zone diameter is estimated is 45 and 39 μm along X- and Y-axis respectively.

4.4.3 Measurable Flow Range

The measurable flow range of the multi-parametric PAM is co-determined by the pulse repetition rate of the laser and the B-scan rate. [41] Before *in vivo* applications, this range was examined in a vessel-mimicking phantom. [41,72] Specifically, deliberated bovine blood (910,

Quad Five) in a plastic tube (56514, United States Plastic Corporation) was driven to flow at 22 different preset speeds by a syringe pump (NE-300, Pump System). The flow speeds of the bovine blood were measured by the high-speed multi-parametric PAM and compared with the preset values. Linear regression analysis revealed a strong linear relationship (R^2 = 0.98) between the measured and preset flow speeds within the range of 0.2 to 8 mm/s (Fig. 4.5).

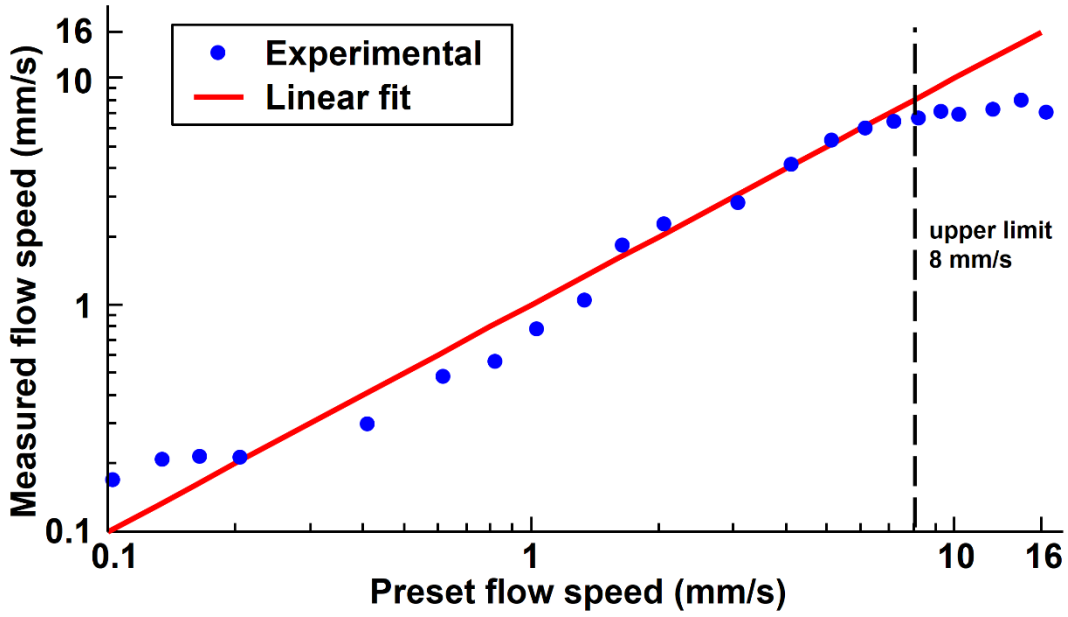

Fig. 4.5 Examination of the measurable flow range in blood phantom. The measurable flow range is estimated as 0.2-8 mm/s.

Similar to our previous multi-parametric PAM, the upper limit of the measurable flow range is determined by the time interval between two contiguous A-lines in the same B-scan. The smaller the interval, the faster the decorrelation it can sample for the correlation analysis. In our current high-speed multi-parametric PAM system, the average interval is ~0.24 ms due to the 2.1-kHz

round-trip rate of the galvanometer scanner. This upper limit can be readily improved by using a resonant galvanometer scanner, whose round-trip rate is as high as 12 kHz (e.g., 6SC12KA040-04Y, Cambridge Technology). With that, we can push the limit to ~50 mm/s. The lower limit is determined by the 5.7-ms correlation window, as shown in Fig. 4.2(b). The time window is not wide enough to fully record slow decays induced by extremely low speeds. This lower limit can be extended by reducing the B-scan rate at the expense of the imaging time.

4.4.4 High-speed Multi-parametric PAM of the Mouse Brain *in vivo*

Upon examining the performance of the high-speed multi-parametric PAM *in vitro*, we further tested its *in-vivo* performance in the mouse brain. As shown in Fig. 4.6, the C_{Hb}, sO_2, and CBF of individual microvessels were simultaneously imaged over a ~3-mm-diameter cortical region through the thinned-skull window. The image SNR is comparable to that acquired by conventional PAM [40]. Average filter was applied to smooth all the measurement results. The functional measurement results matched other published results [30,70] very well. The imaging penetration depth was estimated to be ~250 μm. The pulse energies applied to the mouse brain were 85 and 95 nJ at 532 and 558 nm, respectively. The total image acquisition time was ~10 minutes. In this experiment, we did not monitor the laser absorption induced localized temperature change, however, due to the high incident laser power (27 mW), we expect the tissue temperature will be increased.

The imaging speed of the hybrid scan-based multi-parametric PAM is currently limited by the acoustic focal zone and is insufficient to visualize rapid CBF changes in response to the brain stimulation. Within the 40-μm focal diameter, 20 dual-wavelength B-scans are acquired with an average interval of 2 μm, which is much smaller than the 10-μm B-scan interval used in our

previous multi-parametric PAM and the MEMS-based high-speed PAM. Expanding the focal diameter along the Y-axis to 200 μm by a cylindrically focused transducer will allow us to spread the 20 B-scans with a 10-μm interval, thereby improving the speed by 5-fold. Also, the correlation-based CBF measurement limits the B-scan rate to 0.88 mm/s. In applications where only vascular anatomy and sO_2 are of interest, the B-scan rate can be increased to 10 mm/s, which can further improve the imaging speed by an order of magnitude.

Also, the axial resolution of the reported system is currently limited by the bandwidth of the ultrasonic transducer to ~50 μm. It cannot resolve overlapping vessels within this focal zone, which may affect the accuracy of the hemodynamic readouts. This limitation can be addressed by increasing the bandwidth of the ultrasonic detection [24,73].

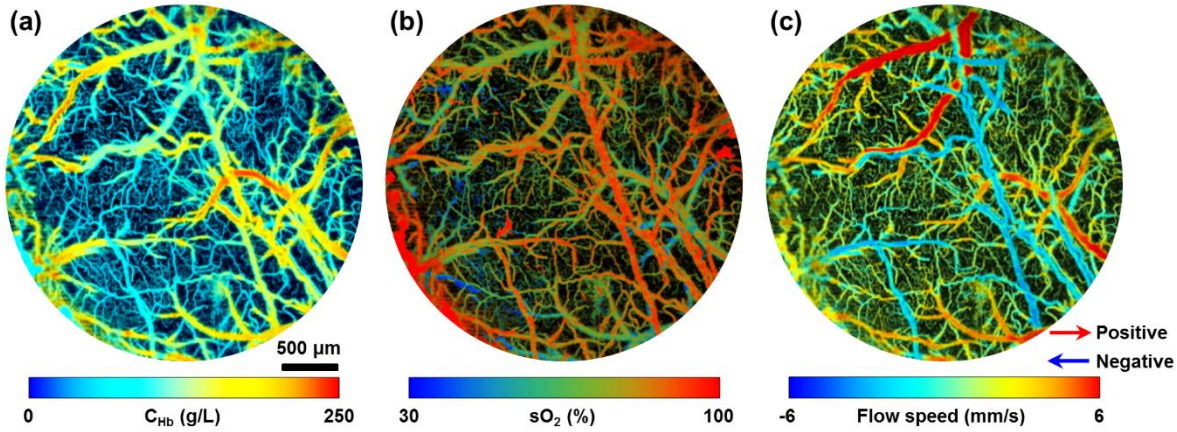

Fig. 4.6 Simultaneous high-speed PAM of (a) C_{Hb} (b) sO_2 (c) CBF in the mouse brain. The image acquisition time was ~10 mins and the image penetration depth was ~250 μm. The functional measurement results match those of published results [40,62].

4.5 Summary

We have developed a new generation of multi-parametric PAM with an unprecedented A-line rate of 300-kHz. By integrating the high-repetition dual-wavelength Raman laser and the optical-mechanical hybrid scan, this technology innovation enables simultaneous high-resolution PAM of C_{Hb}, sO_2, and CBF at a speed 20-time faster than that of the previous generation [41]. Expanding the focal zone of the acoustic detection is expected to improve the imaging speed by another 5-fold. Envisioned applications of this technique include longitudinal monitoring of hemodynamic and metabolic dysfunctions in ischemic stroke, traumatic brain injury, and Alzheimer's disease.

Chapter 5

Ultra-high Speed Photoacoustic Microscopy with A-line Rate of 1.2-MHz

5.1 Introduction

In chapter 4, we introduced a high-speed multi-parametric PAM with A-line rate of 300-kHz. The high speed PAM is capable of measuring C_{Hb}, sO_2 and CBF simultaneously *in vivo* and acquire a 3-mm diameter image within 10 minutes. Although encouraging, there are several factors limit its practical usage. First, the 10 minutes image acquisition time is still not short enough for monitoring acute cerebral hemodynamics, for example, epilepsy happens within one minute, brain response to external stimulation happens within several seconds. Second, the upper bound of flow measurement is 8 mm/s which is sufficient in most physiology studies. However, when animal are under abnormal condition or stimulation, their CBF may increase and potentially exceed the upper bound of the imaging system, leading to measurement inaccuracy. To address these problems, we designed and developed an ultra-high speed multi-parametric PAM with A-line rate of 1.2-MHz. By employing two 600-kHz PRR lasers and a weakly focused ultrasound transducer with 250-μm acoustic focal zone diameter, we effectively expanded the optical scan range from 40-μm to 250-μm and achieved 6-fold imaging speed improvement over the 300-kHz PAM. Moreover, we

employed a resonant optical scanner which can achieve 12 kHz optical scan frequency. This pushes the maximum measurable flow speed to be 33 mm/s which is about 4 times of the 300-kHz PAM. With such performance, we can measure CBF accurately even the flow speed becomes very fast. This outstanding performance provides us a method to study cerebral hemodynamic response to external stimulation or other transient physiology phenomena.

5.2 Materials and Methods

5.2.1 Experimental Setup

As shown in Fig. 5.1, the ultra-high speed PAM consisted of two parts, a dual-wavelength laser and a scan head. The dual-wavelength laser employed two 532-nm nanosecond pulsed laser (GLPM-20-Y13, IPG Photonics) with pulse duration of 1.2 ns and PRR of 600 kHz respectively. The output beam from laser #1 was coupled into an SMF (P1-460B-FC-2, Thorlabs) through a collimator (CFC-11X-A, Thorlabs) directly and transmitted to scan head. A HWP (WPH05M-532, Thorlabs) and a PBS (PBS102, Thorlabs) were placed in front of the collimator to act as an attenuator to adjust the incident laser pulse energy. The output beam from laser #2 was coupled into a pure silica core PM-SMF (HB450-SC, Fibercore) via a collimator (CFC-11X-A, Thorlabs) to realize SRS based wavelength conversion. The pure silica core PM-SMF can resist photo darkening and survive from the strong incident laser pulse energy [74]. The coupling efficiency was 60%. A HWP (WPH05M-532, Thorlabs) and a PBS (PBS102, Thorlabs) was placed in front of the collimator (CFC-11X-A, Thorlabs) to adjust the incident pulse energy. The output beam from PM-SMF was collimated by a collimator (CFC-11X-A, Thorlabs) and passed through a BPF (et560/10bp) to purify the 558-nm component. According to our measurement, when the incident

beam energy was 1.1 μJ, the pulse energy of 558-nm laser can achieve its maximum value of 350 nJ. The 558-nm beam was finally coupled into an SMF (P1-460B-FC-2, Thorlabs) via another collimator (CFC-11X-A, Thorlabs) to be delivered to the scan head. On the scan head, the 532-nm laser and 558-nm laser emitted from the two SMFs were collimated by an achromatic doublet firstly (AC127-025-A, Thorlabs) and combined on a dichroic mirror (FF538-FDi01, Semrock). The combined beam was steered by a resonant scanner (CRS SYSTEM 12K, Cambridge Technology) to realize optical scan along Y-axis. The steered light was focused on the imaging target by an achromatic doublet (AC127-025-A, Thorlabs). A correction-lens (LA1207-A, Thorlabs) was also inserted into the optical path to compensate for the optical aberration at the water-air interface. A piece of thin transparent glass (thickness: 550 μm) was inserted into the optical path to reflect the excited ultrasound signal into the weakly focused transducer. According to our measurement, the FWHM of the transducer focal zone was 250-μm [Fig. 5.1(b)] which defines the optical scanning range. Before imaging, optical-acoustic confocal was achieved by carefully alignment of all the optical components. The detected ultrasound signal was amplified and then digitized by our waveform digitizer (ATS9350, AlazarTech). The entire imaging head was mounted on a two-axis motorized linear stage (PLS-85, PI miCos) for 2D mechanical scan. A homemade water tank was used to immerse the transducer and the correction lens. A thin layer of ultrasound gel (Aquasonic CLEAR®, Parker Laboratories) was sandwiched between the object to be imaged and the transparent polyethylene membrane at the bottom of the water tank for acoustic coupling. An FPGA (PCIe-7842R, National Instruments) was used to synchronize the laser, resonant scanner, linear stages, and waveform digitizer during image acquisition. During image acquisition, the data stream speed can achieve as high as 700 MB/s. To avoid memory overflow, a RAID 0 consists of 3 solid-state-drive (SSD) was employed to meet the data writing requirement.

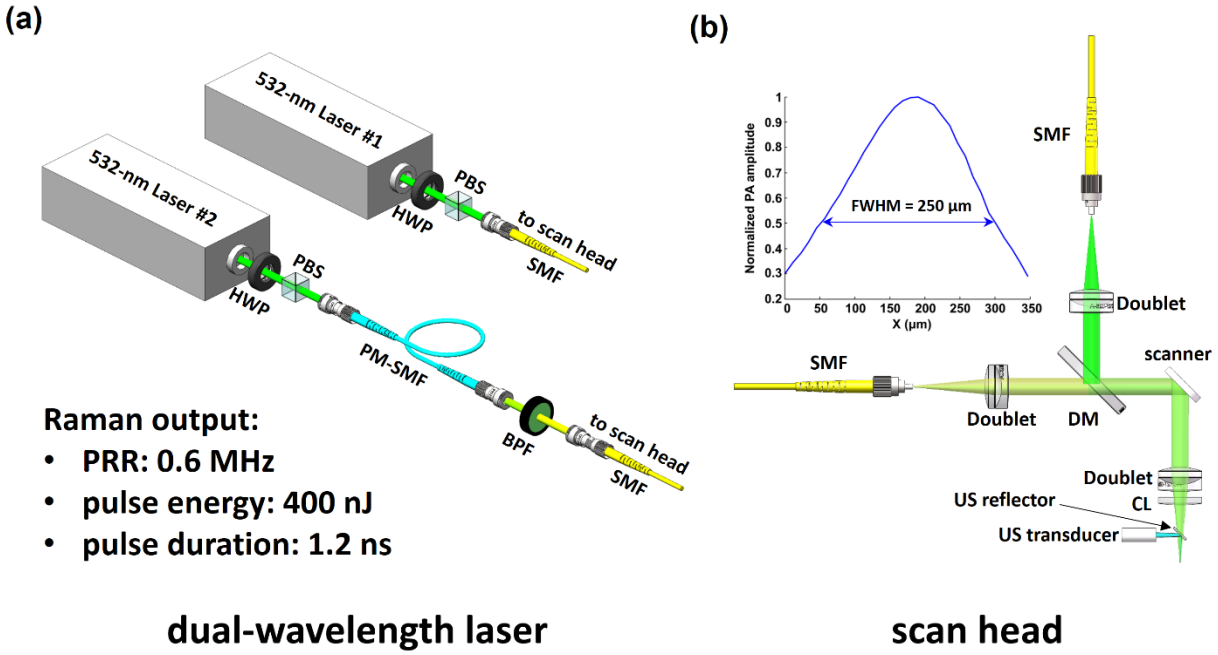

Fig. 5.1. Schematic of the ultra-high speed multi-parametric PAM. (a). Dual-wavelength laser. HWP, half-wave plate; PBS, polarizing beam splitter; PM-SMF, pure silica core polarization-maintaining single-mode fiber; BPF, bandpass filter; SMF, regular single-mode fiber; (b). Scan head. DM, dichroic mirror; BSA, beam sampler; CL, correction lens.

5.2.2 Scanning Mechanism and Measurement Principle

The scan and measurement principle follows that of 300-kHz PAM [59]. The scan mechanism employs optical-mechanical hybrid scan mode. As shown in Fig.5.2, the resonant scanner steers the laser spot scan along the Y-axis within the acoustic focus of the transducer at a round-trip rate of 12 kHz as the linear stage mechanically translates the optical-acoustic dual foci along the X-axis at a constant speed of 1 mm/s. For each laser, the optical scan pattern is a sinusoidal function. As shown in the blow up of Fig. 5.2, after carefully adjustment the initial phase of the sinusoidal function, the pixels of first-half cycle and pixels of second-half cycle are evenly distributed along

Y-axis with space interval of ~10-μm. Since the X-interval between the first-half cycle and second-half cycle is much smaller than the optical focus, we consider them have the same X-coordinate. To assure an approximately constant pixel size along the Y-axis, for each wavelength, only the 25 pixels near the center of the optical scan are extracted for image reconstruction. Thus, 25 dual-wavelength B-scans can be simultaneously acquired, with the optical scan range of 250-μm, leading to a 25-fold increase in the imaging speed over our previously reported conventional multi-parametric PAM, and 6-fold imaging speed improvement over the 300-kHz PAM. The principle of C_{Hb} measurement, sO_2 measurement and CBT measurement follows exactly those of 300-kHz PAM. In this system, the time interval of adjacent A-lines in one B-scan is 0.083 ms, thus when the translation stage moves 10 μm distance, 120 A-lines will be acquired for both C_{Hb} and CBF measurement. Also, compared to the 0.24 ms time interval of adjacent A-lines in one B-scan in 300-kHz PAM, the shortened time interval in the ultra-high speed PAM guarantees enough sampling point in the flow-induced decorrelation curve so that the system can distinguish different flow speed when CBF is very high.

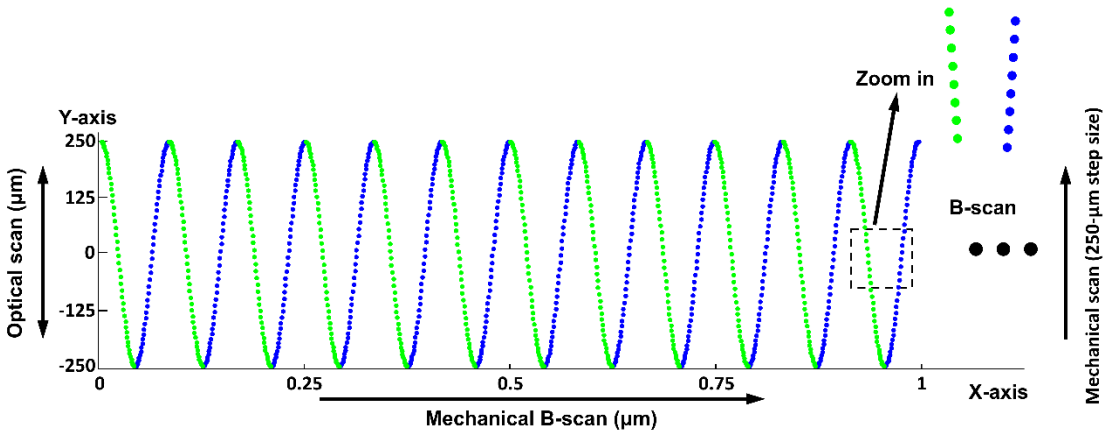

Fig. 5.2 Scan scheme of ultra-high speed PAM. The scan pattern follows that described in 4.2.2. The initial phase of the sinusoidal function is carefully adjusted so that the pixels of first half cycle and pixels of second half cycle are evenly distributed along Y-axis with space interval of ~10 μm.

5.3 Results

5.3.1 Measurable Flow Range

Before *in vivo* applications, the measurable flow range was examined in a vessel-mimicking phantom. The experimental setup has been described in 4.4.3. Linear regression analysis revealed a strong linear relationship between the measured and preset flow speeds within the range of 1 to 33 mm/s (Fig. 5.3). Compared to the 300-kHz PAM, the upper limit of measurable blood flow speed is increased by 4-fold. This is because the use of resonant scanner shortened the time interval between adjacent A-lines in one B-scan from 0.24 ms to 0.083 ms so that the system can measure the decay rate of decorrelation curve when flow speed is fast. Such high dynamic range guarantees that our ultra-high speed PAM can study blood flow speed response to external stimulation.

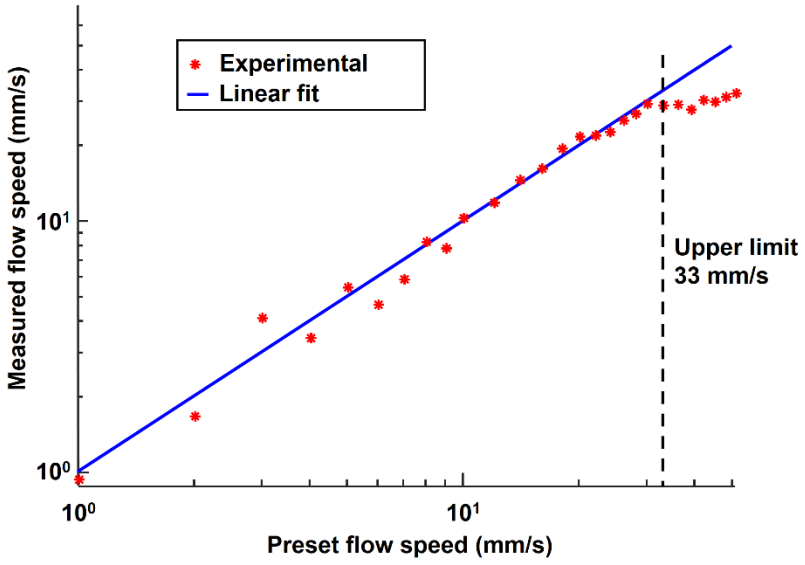

Fig. 5.3 Flow calibration curve of ultra-high PAM. The measurable flow range is estimated to be 1–33 mm/s.

5.3.2 Validation of Ultra-high Speed PAM

After the system was developed, we performed simultaneous measurement of cerebral vasculature, sO_2 and CBF of mouse brain *in vivo* by using both our previously well-developed muti-parametric PAM and the ultra-high speed PAM to validate the new system. Before imaging, a male CD1 mouse (17 weeks old) was used for the *in vivo* study. For optimal imaging quality, the mouse skull above the right somatosensory cortex was thinned to ~100 μm prior to the PAM experiment, forming a circular imaging window with a diameter of ~3 mm. Throughout the PAM experiment, the mouse was maintained under anesthesia with 1.0–1.5% isoflurane and the body temperature was kept at 37 °C using a temperature-controlled heating pad (EW-89802-52, Cole-Parmer; SRFG-303/10, Omega). All experimental procedures were carried out in conformity with the laboratory animal protocol approved by the Animal Care and Use Committee at the University of Virginia. As shown in Fig. 5.4, the cerebral vasculature image from both PAM system shows comparable SNR and resolution. The functional measurement of sO_2 and CBF shows similar results as well.

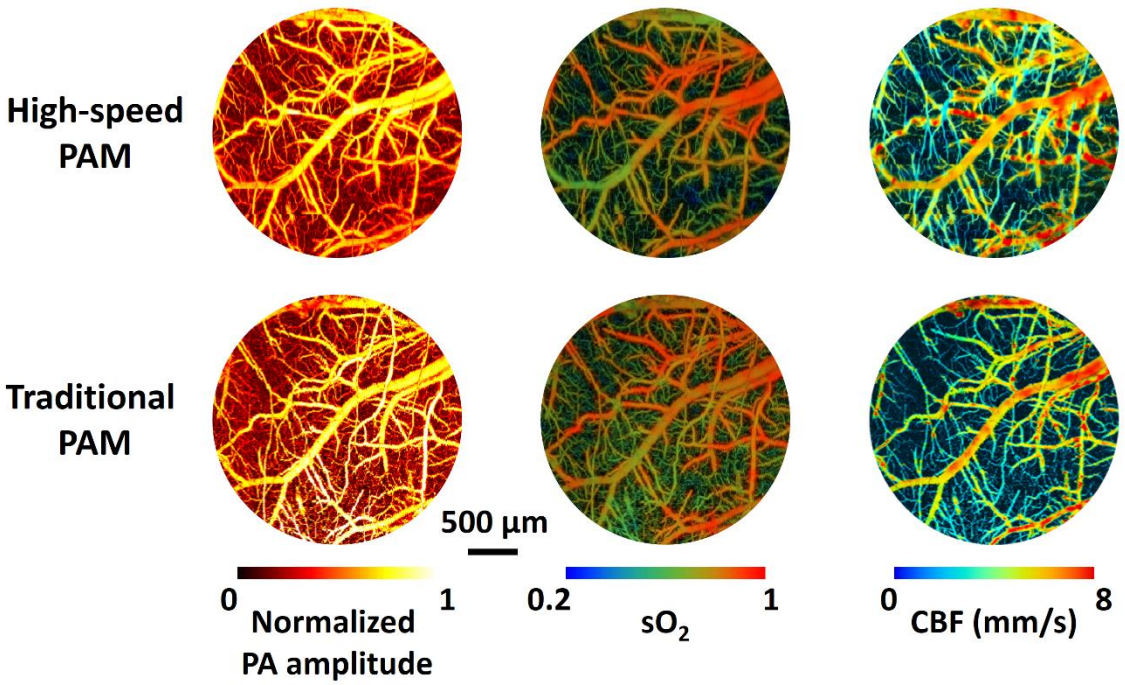

Fig. 5.4 Measurement of cerebral vasculature, sO_2 and CBF by using both traditional PAM and ultra-high speed PAM. The vasculature imaged by both PAM show comparable SNR and resolution. The functional measurement of sO_2 and CBF match each other.

5.3.3 PAM of Acute Cerebral Hemodynamics to rIPC

After the ultra-high speed PAM is validated, we applied the system to study acute cerebral hemodynamics to remote ischemia preconditioning (rIPC). rIPC was first demonstrated in cardiac tissue in which brief episodes of myocardial ischemia and reperfusion applied to one vascular territory reduced the infarct size of the adjacent tissue that had not undergone any preconditioning [75–78]. rIPC has primarily been applied to the myocardium as a target organ, but subsequent studies showed that brief ischemia induced in nontarget tissue, most commonly in the limb or arm, confers protection at a remote site such as the brain [79,80], lung [81], kidney [82,83],

intestine [84], or skeletal muscle [85]. Prior to image acquisition, the mouse was properly processed to achieve optimum imaging quality. The detailed procedure has been described in section 5.3.2. After the mouse was properly processed, we applied our ultra-high speed multi-parametric PAM to study cerebral hemodynamics to rIPC. Firstly, hind limb occlusion was performed [80,86]. The occlusion lasted for 5 minutes. During which time, both sO_2 and CBF of mouse brain with a 3×3 mm^2 field of interest were monitored. Four images were acquired within the 5-minute time window. According to the measurement results, the CBF increased at the beginning of the occlusion as a strong response to the procedure, then decreased. After 5 minutes, hind limb reperfusion was performed and another four images were acquired. According to the results, the CBF fluctuated through this time window. Through the entire measurement procedure, sO_2 did not show significant change. The detailed physiology explanation for this phenomena is still an open question. To further validate our measurement result, a control experiment was performed. The mouse was firstly processed exactly as the first mouse to create the optical imaging window and both sO_2 and CBF were maeasured without any procedure. Four images were firstly acquired within the first 5 minutes and then another four images were acquired within the second 5 minutes. According to the results, both sO_2 and CBF showed no observable change through the entire image acquisition. This demonstrates the flow change is due to rIPC.

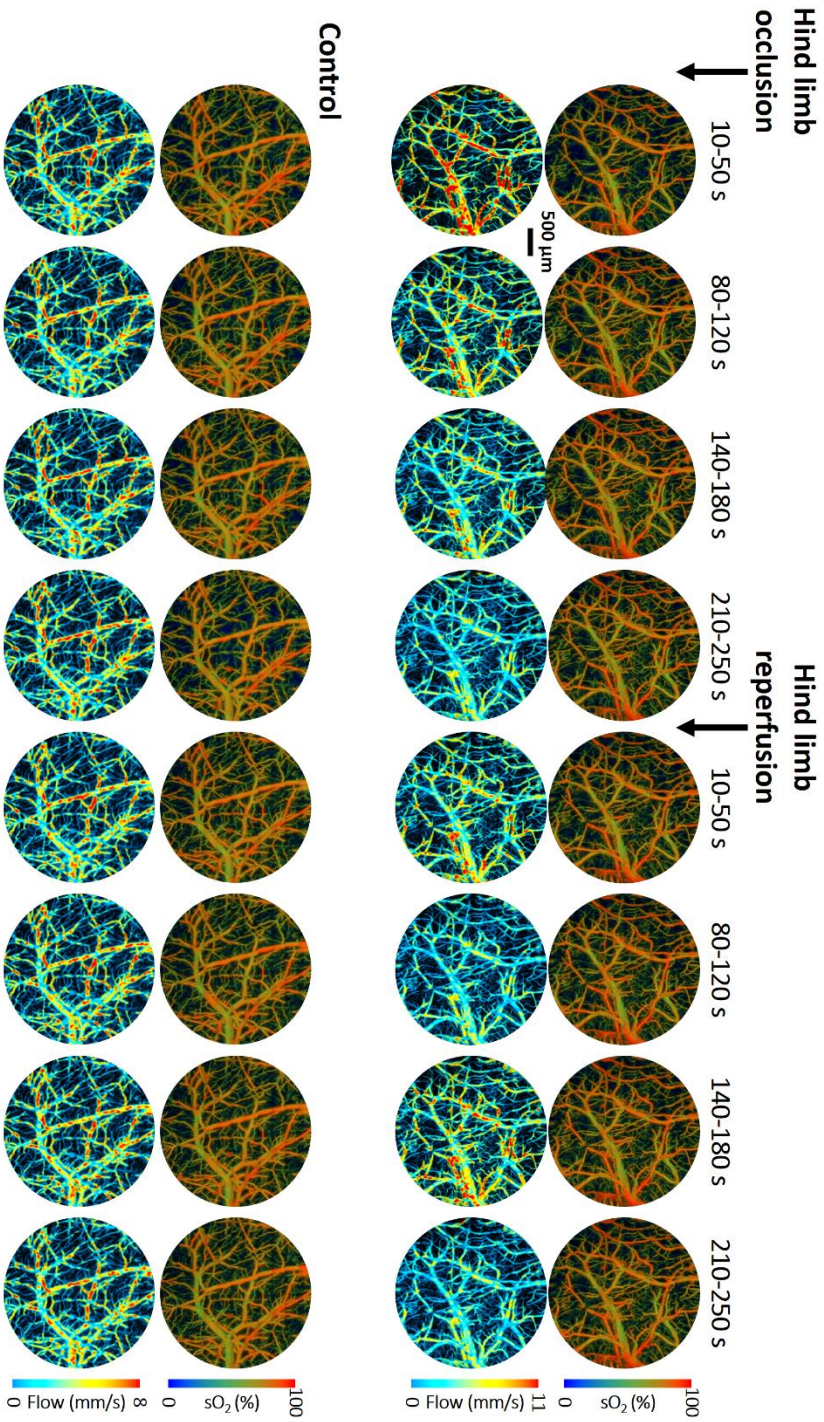

Fig. 5.5 PAM of acute cerebral hemodynamics to rIPC. (a) sO_2 and CBF measurement of mouse brain to rIPC. The CBF increased at the beginning of the occlusion as a strong response to the procedure, then decreased. During reperfusion, the CBF fluctuated through this time window. Through the entire measurement procedure, sO_2 did not show significant change. (b) sO_2 and CBF measurement of mouse brain in control group. Both CBF and sO_2 maintain constant through the entire time window.

5.4 Summary

In summary, we developed an ultra-high speed multi-parametric PAM with A-line rate of 1.2-MHz. By employing two 600 kHz PRR pulsed laser and a weakly focused transducer with 250-μm focal zone diameter, the imaging speed has been improved by more than 6-fold compared to our previously developed high-speed multi-parametric PAM with A-line rate of 300-kHz. By using a resonant scanner with scan frequency of 12 kHz, the maximum measurable blood flow speed of 33 mm/s was achieved. Compared to the 300-kHz PAM, there was a 4-fold improvement. The ultra-high speed PAM was validated by performing an *in vivo* measurement comparison with our previously well-developed multi-parametric PAM. The results demonstrated that the ultra-high speed PAM can achieve comparable SNR and resolution. The functional measurement including sO_2 and CBF acquired by both PAM matched each other as well. Finally, we applied the ultra-high speed PAM to study rIPC. Due to the high imaging speed, we observed the CBF response to rIPC. Future work may include applying the PAM to study cerebral hemodynamic to external stimulation and perform brain related researches such as epilepsy. These studies can help us have a better understanding of the physiological processes.

Chapter 6

Discussion and Future Work

The work presented in this dissertation has demonstrated the design and development of isotropic spatial resolution OR-PAM and high-speed multi-parametric PAM. Two strategies including SPR based broadband ultrasound detector and multi-view image acquisition and deconvolution are presented in chapter 2 and chapter 3 to provide methods to improve the axial resolution in OR-PAM. In chapter 4, dual-wavelength high PRR laser based on SRS effect is introduced, combined with optical-mechanical hybrid scan mode, high-speed multi-parametric PAM with A-line rate of 300-kHz has been developed and demonstrated by *in vivo* imaging of mouse brain. In chapter 5, by further improving laser PRR, ultrasound transducer focal area and optical scanner, ultra-high speed multi-parametric PAM with A-line rate of 1.2-MHz has been developed and validated, acute hemodynamics of mouse brain induced by rIPC has been studied by using the system.

The SPR based ultrasound detector can potentially detect up to GHz ultrasound signal and thus can perform supreme axial-resolution PA imaging. However, the detection sensitivity needs to be further improved. The measured noise equivalent pressure is 3.3 kPa which is more than one order of magnitude worse than that of conventional piezo-transducer. To address this problem, long-range SPR can be a possible solution which could improve the sensitivity by a factor of 5 [55].

Also, replacing water by ethanol as the SPW coupling medium can further improve the sensitive by a factor of 3. Moreover, we can perform signal average of adjacent A-lines to improve SNR, however this approach may cause dense A-line sampling and thus elongate image acquisition time. Also, SPR-PAM requires the use of an optical prism thus will block the PA excitation light when operating in reflection mode. Therefore, in chapter 2, the device is developed on transmission mode which could be a problem in *in vivo* imaging applications. This problem could possibly be addressed by developing fiber based SPR sensor [87] to detect PA signal.

MAI-PAM utilizes multiple illumination light with different angles. With the help of multi-view deconvolution algorithm, the system can reconstruct the image with isotropic spatial resolution. One issue in this implementation is that the number of views should be further optimized. Theoretically, two views will be sufficient to achieve isotropic spatial resolution. However, according the simulation results in Fig. 3.2, MAI-PAM with only two views has very strong artefact that induced by the scattered photon absorption and the algorithm itself. To reduce this effect, we finally employed a three-view scheme. According to both the phantom and *in vivo* experimental results, the reconstructed images show better resolution isotropy and quality than images acquired by conventional PAM. However, we should notice that when the absorber become much denser, the three-view scheme may also suffer from artefacts. To address this problem, we should add more views. Besides the number of views, SNR is another factor that affects the image reconstruction. According to our simulation, in the three-view setup, when the SNR of each individual view is lower than 2:1, the reconstructed image suffers from severe artefacts. Thus, during imaging, high SNR must be achieved, this can be easily guaranteed by increasing laser pulse energy.

Another issue of MAI-PAM is the slow imaging speed. Currently, the system performs mechanical scan along three axis. Moreover, to guarantee image reconstruction quality and resolution isotropy, the image acquisition requires high sampling frequency along both X and Z axis. Thus, the imaging speed is severely limited. For example, the *in vivo* imaging of mouse ear experiment introduced in 3.4.2 has $300 \times 500 \times 200\ \mu m^3$ field of interest which takes ~ 5 hours for image acquisition. To improve imaging speed, we can apply optical-mechanical hybrid scan. As shown in Fig. 6.1, on the scan head, the output beam from SMF_1, SMF_2 and SMF_3 corresponding to the illumination beam of $view_1$, $view_2$ and $view_3$ are collimated by a lens, steered by an optical scanner. The beam from SMF_1 and SMF_3 are reflected by another mirror and then focused onto the tissue by an optical lens. The beam from SMF_2 is focused onto the tissue directly by an optical lens. A ring shaped ultrasound transducer is employed to detect PA signal for all the three views. The scan mechanism follows that of high-speed multi-parametric PAM. Assuming the diameter of transducer focal zone is 40-μm, the imaging speed can be improved by a factor of 48.

The current MAI-PAM cannot perform functional measurement. To realize sO_2 measurement, another wavelength of 558 nm can be added to each view. With the help of multi-view deconvolution algorithm and spectral analysis, the system can potentially measure sO_2 with isotropic spatial resolution.

Beside the above mentioned two methods, nonlinear absorption based PAM is also a potential approach to solve the resolution anisotropy problem. Unlike conventional PAM which defines its axial resolution by its ultrasound detection bandwidth, nonlinear optical absorption happens only in the optical focal volume and thus the axial resolution can be confined by tightly focused light. Using a high NA optical objective, the axial resolution can achieve micron-level. Several approaches including photo bleach [88] based PAM, Grueneisen relaxation PAM [89], transient

absorption ultrasonic microscopy [90] and two photon PAM [91,92] have been studied and demonstrated.

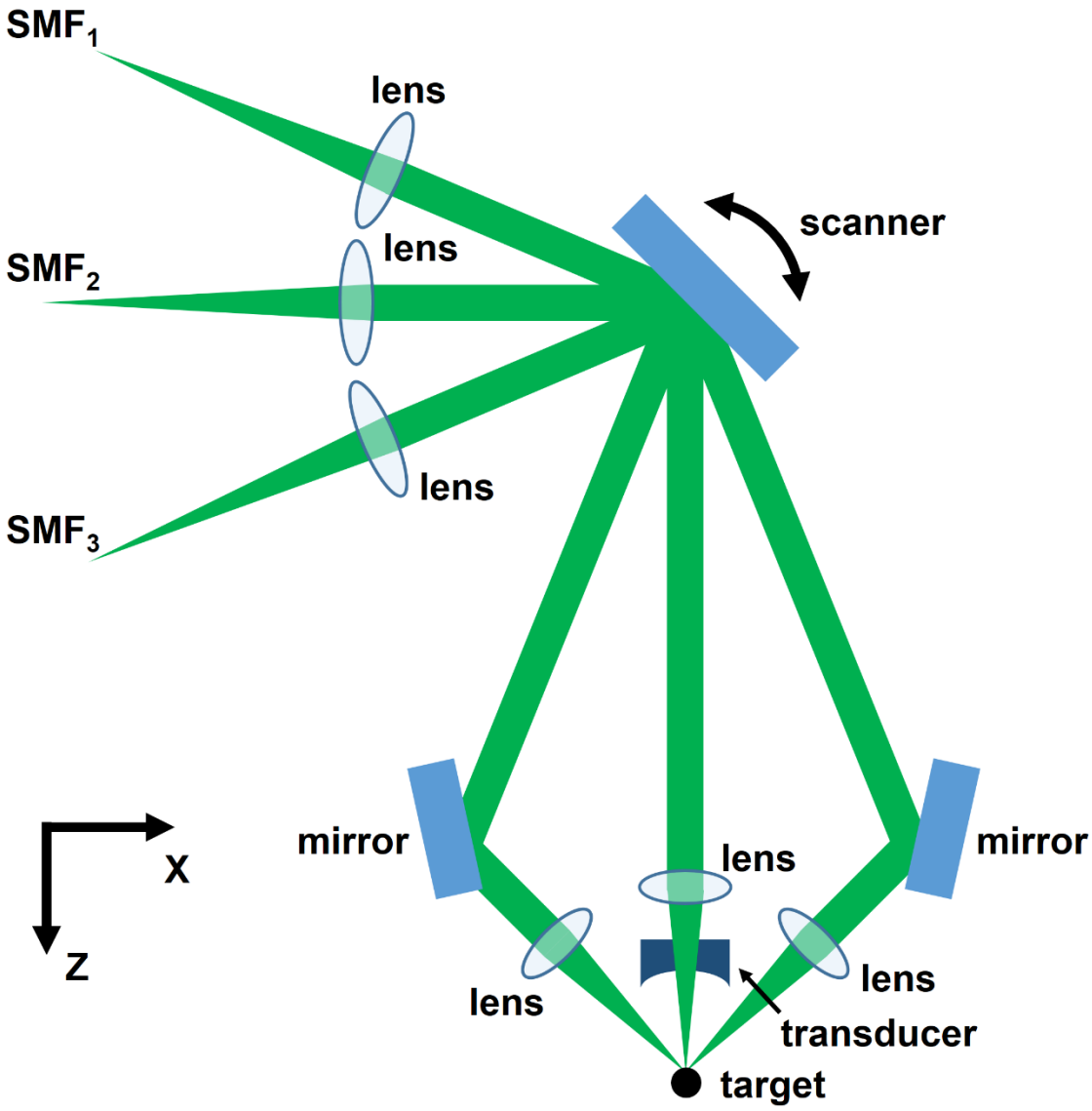

Fig. 6.1 Schematic of MAI-PAM in optical-mechanical hybrid scan mode. SMF, single mode fiber

The isotropic resolution PAM can provide a new method in neuron science. For example, the thickness of molecular layer in mouse brain is tens of micron which is comparable to the axial resolution of conventional PAM. Thus to study the physiological processes in molecular layer, PAM with isotropic resolution will be useful.

As in high speed multi-parametric PAM, there are two factors limit the imaging speed, laser PRR and limited transducer focal zone. Currently, high PRR 532-nm lasers are commercially available and widely used, however, to realize sO_2 measurement, dual-wavelength laser is required. To address this problem, we adopted SRS based wavelength conversion by using a PM-SMF. According to our measurement result, with 1.2 ns laser pulse duration and 10-meter long PM-SMF, ~60% 532-nm photon can be converted to 558-nm photon in the fiber, and we achieved maximum output of 350-nJ 558-nm pulse energy. This is more than enough in PAM and enables us to realize high speed multi-parametric PAM. To overcome the transducer focal zone limit, we employed a weakly focused ultrasound transducer with focal zone diameter of 250 μm. According to our measurement result, the PA detection sensitivity is half of the tightly focused ring shaped transducer which is employed in our conventional PAM [41,59] and the high speed multi-parametric PAM with A-line rate of 300-kHz. However the weakly focused transducer can increase the focal zone diameter by 6-fold which enlarges optical scan range by 6-fold. As shown in Fig. 5.4, the decreased detection sensitivity does not affect our image quality very much while allows 6-fold imaging speed improvement.

One potential issue in the ultra-high speed multi-parametric PAM is the use of high optical power. Considering the 1.2-MHz laser PRR and 100-nJ laser pulse energy, the optical power used is 120 mW during image acquisition. According to our experimental test, such optical power is still safe, however, further increasing the optical power to ~150 mW will cause tissue damage.

Thus, to guarantee imaging safety, we should decrease the optical power while maintain image quality. First, we can use an optical switch to reduce the pulse number of 558-nm laser. For example, if we reduce 90% of 558-nm laser pulses, there will be one pair of 532- and 558-nm laser pulses per 5/6 μm. Such sampling frequency will be enough for sO_2 measurement. Also, the optical scan pattern is a sinusoidal function and only the pixels within the linear range are employed for image reconstruction. Thus another optical switch can be employed to remove all the laser pulses that fall in the nonlinear range. With these two approaches, the optical power can be reduced from 120 mW to 33 mW. Meanwhile, since the laser pulse energy is maintained, the signal SNR will not be affected.

Another issue in ultra-high speed multi-parametric PAM is, due to the wide optical scan range, the system cannot acquire the true flow speed by applying bi-directional scan analysis as described in 4.2.2. Thus the measured flow speed may include the influence from the speed of translation state and is not accurate to measure blood flow speed that is close or lower than 1 mm/s. There are two ways to address this problem. The first method is scanning the same B-scan twice with opposite mechanical scan direction along X-axis, in this case, we can apply the bi-directional scan analysis described in 4.2.2 and reveal the true blood flow speed. The second method is applying M-mode scan, in which we do optical scan with 100 cycles to acquire 100 A-lines per pixel for flow measurement, during the optical scanning, we keep the translation stage static so that the measured flow speed will not be influenced by the translation stage thus can reveal the true flow speed, after the optical scan, we move the X-axis translation stage with a certain step size and repeat the optical scan. Both methods can measure low blood speed effectively with the price of elongated image acquisition time.

To further improve the imaging speed, we can adopt laser with higher PRR and transducer with broader focal zone area. By decreasing optical power to ensure imaging safety, such improvement can be potentially realized.

We can also apply the ultra-high speed multi-parametric PAM to perform physiology studies including observing cerebral hemodynamics under external stimulation and acute cerebral hemodynamics induced by rIPC.

Beside the above mentioned high-speed multi-parametric PAM, Yao *et al*. presents a high speed PAM by using single wavelength light source with different pulse duration. The sO_2 measurement is based on the absorption saturation effect of HbO_2 [30,93,94]. Moreover, the PAM utilizes a water immersible microelectromechanical systems (MEMS) to steer both the PA excitation light and excited PA wave. In this case, the optical scan range is no longer limited by ultrasound transducer focal zone since optical-acoustic confocal can always be satisfied during scanning. However, such optical scanner cannot achieve high scanning frequency and is not suitable for flow measurement.

The above mentioned technique can address resolution anisotropy and imaging speed problem separately. Our ultimate goal is to achieve a high speed multi-parametric PAM with isotropic spatial resolution. One potential solution is to combine PAM with OCT [95] By detecting the refractive index change induced by PA signal by using OCT, the system can benefit the high-axial resolution nature of OCT. Also, the system will be pure optical, so the imaging acquisition time will be comparable to that of OCT.

References

1. L. V. Wang and Hsin-I Wu, *Biomedical Optics: Principles and Imaging* (2012).

2. M. Oheim, E. Beaurepaire, E. Chaigneau, J. Mertz, and S. Charpak, "Two-photon microscopy in brain tissue: Parameters influencing the imaging depth," J. Neurosci. Methods (2001).

3. J. B. Pawley, "Confocal and two-photon microscopy: Foundations, applications and advances," Microsc. Res. Tech. (2002).

4. F. Helmchen and W. Denk, "Deep tissue two-photon microscopy," Nat. Methods (2005).

5. W. Drexler, U. Morgner, R. K. Ghanta, F. X. Kärtner, J. S. Schuman, and J. G. Fujimoto, "Ultrahigh-resolution ophthalmic optical coherence tomography," Nat. Med. (2001).

6. M. R. Hee, C. A. Puliafito, C. Wong, J. S. Duker, E. Reichel, B. Rutledge, J. S. Schuman, E. A. Swanson, and J. G. Fujimoto, *Quantitative Assessment of Macular Edema with Optical Coherence Tomography.* (1995).

7. M. Wojtkowski, R. Leitgeb, A. Kowalczyk, T. Bajraszewski, and A. F. Fercher, "In vivo human retinal imaging by Fourier domain optical coherence tomography," J. Biomed. Opt. (2002).

8. M. Xu and L. V. Wang, "Photoacoustic imaging in biomedicine," Rev. Sci. Instrum. (2006).

9. L. V. Wang and S. Hu, "Photoacoustic tomography: in vivo imaging from organelles to

organs.," Science (80-.). **335**, 1458–62 (2012).

10. A. Rosencwaig, "Photoacoustic spectroscopy of solids," Phys. Today (1975).

11. G. P. Luke, D. Yeager, and S. Y. Emelianov, "Biomedical applications of photoacoustic imaging with exogenous contrast agents," Ann. Biomed. Eng. (2012).

12. A. De La Zerda, C. Zavaleta, S. Keren, S. Vaithilingam, S. Bodapati, Z. Liu, J. Levi, B. R. Smith, T. J. Ma, O. Oralkan, Z. Cheng, X. Chen, H. Dai, B. T. Khuri-Yakub, and S. S. Gambhir, "Carbon nanotubes as photoacoustic molecular imaging agents in living mice," Nat. Nanotechnol. (2008).

13. S. Mallidi, T. Larson, J. Tam, P. P. Joshi, A. Karpiouk, K. Sokolov, and S. Emelianov, "Multiwavelength photoacoustic imaging and plasmon resonance coupling of gold nanoparticles for selective detection of cancer," Nano Lett. (2009).

14. S. Mallidi, G. P. Luke, and S. Emelianov, "Photoacoustic imaging in cancer detection, diagnosis, and treatment guidance," Trends Biotechnol. (2011).

15. L. V. Wang, "Multiscale photoacoustic microscopy and computed tomography," Nat. Photonics (2009).

16. A. P. Jathoul, J. Laufer, O. Ogunlade, B. Treeby, B. Cox, E. Zhang, P. Johnson, A. R. Pizzey, B. Philip, T. Marafioti, M. F. Lythgoe, R. B. Pedley, M. A. Pule, and P. Beard, "Deep in vivo photoacoustic imaging of mammalian tissues using a tyrosinase-based genetic reporter," Nat. Photonics **9**, 239–246 (2015).

17. X. L. Deán-Ben, T. F. Fehm, S. J. Ford, S. Gottschalk, and D. Razansky, "Spiral volumetric optoacoustic tomography visualizes multi-scale dynamics in mice," Light Sci.

Appl. **6**, (2017).

18. M. Toi, Y. Asao, Y. Matsumoto, H. Sekiguchi, A. Yoshikawa, M. Takada, M. Kataoka, T. Endo, N. Kawaguchi-Sakita, M. Kawashima, E. Fakhrejahani, S. Kanao, I. Yamaga, Y. Nakayama, M. Tokiwa, M. Torii, T. Yagi, T. Sakurai, K. Togashi, and T. Shiina, "Visualization of tumor-related blood vessels in human breast by photoacoustic imaging system with a hemispherical detector array," Sci. Rep. **7**, (2017).

19. S. Hu, K. Maslov, and L. V Wang, "Second-generation optical-resolution photoacoustic microscopy with improved sensitivity and speed.," Opt. Lett. **36**, 1134–1136 (2011).

20. C. Zhang, K. Maslov, and L. V. Wang, "Subwavelength-resolution label-free photoacoustic microscopy of optical absorption in vivo," Opt. Lett. **35**, 3195–7 (2010).

21. L. V. Wang, "Tutorial on photoacoustic microscopy and computed tomography," IEEE J. Sel. Top. Quantum Electron. (2008).

22. H. F. Zhang, K. Maslov, M. Sivaramakrishnan, G. Stoica, and L. V. Wang, "Imaging of hemoglobin oxygen saturation variations in single vessels in vivo using photoacoustic microscopy," Appl. Phys. Lett. **90**, 053901 (2007).

23. K. Maslov, H. F. Zhang, S. Hu, and L. V. Wang, "Optical-resolution photoacoustic microscopy for in vivo imaging of single capillaries," Opt. Lett. **33**, 929 (2008).

24. C. Zhang, K. Maslov, J. Yao, and L. V Wang, "In vivo photoacoustic microscopy with 7.6-μm axial resolution using a commercial 125-MHz ultrasonic transducer.," J. Biomed. Opt. **17**, 116016 (2012).

25. H. F. Zhang, K. Maslov, G. Stoica, and L. V. Wang, "Functional photoacoustic

microscopy for high-resolution and noninvasive in vivo imaging," Nat. Biotechnol. **24**, 848–851 (2006).

26. S. Park, C. Lee, J. Kim, and C. Kim, "Acoustic resolution photoacoustic microscopy," Biomed. Eng. Lett. (2014).

27. J. Yao, J. Xia, K. I. Maslov, M. Nasiriavanaki, V. Tsytsarev, A. V. Demchenko, and L. V. Wang, "Noninvasive photoacoustic computed tomography of mouse brain metabolism in vivo," Neuroimage (2013).

28. J. Xia, M. R. Chatni, K. Maslov, Z. Guo, K. Wang, M. Anastasio, and L. V. Wang, "Whole-body ring-shaped confocal photoacoustic computed tomography of small animals in vivo," J. Biomed. Opt. (2012).

29. M. Xu and L. V. Wang, "Universal back-projection algorithm for photoacoustic computed tomography," Phys. Rev. E - Stat. Nonlinear, Soft Matter Phys. **71**, (2005).

30. J. Yao, L. V. L. Wang, J.-M. Yang, K. I. Maslov, T. T. W. Wong, L. Li, C.-H. Huang, J. Zou, and L. V. L. Wang, "High-speed label-free functional photoacoustic microscopy of mouse brain in action," Nat. Methods **12**, 407–+ (2015).

31. J. Y. Kim, C. Lee, K. Park, G. Lim, and C. Kim, "Fast optical-resolution photoacoustic microscopy using a 2-axis water-proofing MEMS scanner," Sci. Rep. (2015).

32. T. Liu, Q. Wei, J. Wang, S. Jiao, and H. F. Zhang, "Combined photoacoustic microscopy and optical coherence tomography can measure metabolic rate of oxygen," Biomed. Opt. Express (2011).

33. J. Yao, K. I. Maslov, Y. Zhang, Y. Xia, and L. V. Wang, "Label-free oxygen-metabolic

photoacoustic microscopy in vivo," J. Biomed. Opt. (2011).

34. Y. Zhou, J. Yao, K. I. Maslov, and L. V. Wang, "Calibration-free absolute quantification of particle concentration by statistical analyses of photoacoustic signals *in vivo*," J. Biomed. Opt. **19**, 037001 (2014).

35. L. J. Guo, "Nanoimprint Lithography: Methods and Material Requirements," Adv. Mater. **19**, 495–513 (2007).

36. D.-K. Yao, R. Chen, K. I. Maslov, Q. Zhou, and L. V Wang, "Optimal ultraviolet wavelength for in vivo photoacoustic imaging of cell nuclei.," J. Biomed. Opt. **17**, 056004 (2012).

37. D.-K. Yao, K. Maslov, K. K. Shung, Q. Zhou, and L. V Wang, "In vivo label-free photoacoustic microscopy of cell nuclei by excitation of DNA and RNA.," Opt. Lett. **35**, 4139–41 (2010).

38. L. Wang, K. Maslov, and L. V. Wang, "Single-cell label-free photoacoustic flowoxigraphy in vivo," Proc. Natl. Acad. Sci. **110**, 5759–5764 (2013).

39. Y. He, L. V. L. Wang, J. Shi, J. Yao, L. Li, R. Zhang, C. H. Huang, J. Zou, and L. V. L. Wang, "In vivo label-free photoacoustic flow cytography and on-the-spot laser killing of single circulating melanoma cells," Sci. Rep. **6**, (2016).

40. B. Ning, N. Sun, R. Cao, R. Chen, K. K. Shung, J. A. Hossack, J. M. Lee, Q. Zhou, and S. Hu, "Ultrasound-aided Multi-parametric Photoacoustic Microscopy of the Mouse Brain," Sci. Rep. (2015).

41. B. Ning, M. J. Kennedy, A. J. Dixon, N. Sun, R. Cao, B. T. Soetikno, R. Chen, Q. Zhou,

K. Kirk Shung, J. A. Hossack, and S. Hu, "Simultaneous photoacoustic microscopy of microvascular anatomy, oxygen saturation, and blood flow," Opt. Lett. **40**, 910 (2015).

42. P. Hajireza, W. Shi, K. Bell, R. J. Paproski, and R. J. Zemp, "Non-interferometric photoacoustic remote sensing microscopy," Light Sci. Appl. (2017).

43. K. L. Bell, P. Hajireza, W. Shi, and R. J. Zemp, "Temporal evolution of low-coherence reflectrometry signals in photoacoustic remote sensing microscopy," Appl. Opt. (2017).

44. J. Shi, L. V. L. Wang, C. Noordam, and L. V. L. Wang, "Bessel-beam Grueneisen relaxation photoacoustic microscopy with extended depth of field," J. Biomed. Opt. **20**, 116002 (2015).

45. C. Zhang, K. Maslov, S. Hu, R. Chen, Q. Zhou, K. K. Shung, and L. V Wang, "Reflection-mode submicron-resolution in vivo photoacoustic microscopy.," J. Biomed. Opt. **17**, 020501 (2012).

46. C. Zhang, T. Ling, S.-L. Chen, and L. J. Guo, "Ultrabroad Bandwidth and Highly Sensitive Optical Ultrasonic Detector for Photoacoustic Imaging," ACS Photonics **1**, 1093–1098 (2014).

47. H. Li, B. Dong, Z. Zhang, H. F. Zhang, and C. Sun, "A transparent broadband ultrasonic detector based on an optical micro-ring resonator for photoacoustic microscopy.," Sci. Rep. **4**, 4496 (2014).

48. P. C. Beard, F. Perennes, and T. N. Mills, "Transduction mechanisms of the Fabry-Perot polymer film sensing concept for wideband ultrasound detection," IEEE Trans. Ultrason. Ferroelectr. Freq. Control **46**, 1575–82 (1999).

49. R. Nuster, G. Paltauf, and P. Burgholzer, "Comparison of surface plasmon resonance devices for acoustic wave detection in liquid," Opt. Express **15**, 6087 (2007).

50. V. V. Yakovlev, W. Dickson, A. Murphy, J. McPhillips, R. J. Pollard, V. A. Podolskiy, and A. V. Zayats, "Ultrasensitive non-resonant detection of ultrasound with plasmonic metamaterials," Adv. Mater. **25**, (2013).

51. K. Johansen, H. Arwin, I. Lundström, B. Liedberg, I. Lundström, and B. Liedberg, "Imaging surface plasmon resonance sensor based on multiple wavelengths: Sensitivity considerations," Rev. Sci. Instrum. **71**, 3530 (2000).

52. M. Piliarik and J. J. Homola, "Surface plasmon resonance (SPR) sensors: approaching their limits?," Opt. Express **17**, 16505–17 (2009).

53. S. A. Maier, *Plasmonics: Fundamentals and Applications* (n.d.).

54. Z. Xie, S. Jiao, H. F. Zhang, and C. A. Puliafito, "Laser-scanning optical-resolution photoacoustic microscopy," Opt. Lett. **34**, 1771 (2009).

55. G. G. Nenninger, P. Tobiška, J. Homola, and S. S. S. S. Yee, "Long-range surface plasmons for high-resolution surface plasmon resonance sensors," Sensors Actuators B Chem. **74**, 145–151 (2001).

56. G. Paltauf, H. Schmidt-Kloiber, K. P. Köstli, and M. Frenz, "Optical method for two-dimensional ultrasonic detection," Appl. Phys. Lett. **75**, 1048 (1999).

57. L. Zhu, L. Li, L. Gao, and L. V. Wang, "Multiview optical resolution photoacoustic microscopy," Optica **1**, (2014).

58. S. Preibisch, F. Amat, E. Stamataki, M. Sarov, R. H. Singer, E. Myers, and P. Tomancak, "Efficient bayesian-based multiview deconvolution," Nat. Methods **11**, (2014).

59. T. Wang, N. Sun, R. Cao, B. Ning, R. Chen, Q. Zhou, and S. Hu, "Multiparametric photoacoustic microscopy of the mouse brain with 300-kHz A-line rate," Neurophotonics **3**, 045006 (2016).

60. S. Hu, "Neurovascular photoacoustic tomography," Front. Neuroenergetics (2010).

61. S. Hu, "Listening to the Brain With Photoacoustics," IEEE J. Sel. Top. Quantum Electron. **22**, 1–10 (2016).

62. J. Yao, L. Wang, J.-M. Yang, K. I. Maslov, T. T. W. Wong, L. Li, C.-H. Huang, J. Zou, and L. V Wang, "High-speed label-free functional photoacoustic microscopy of mouse brain in action," Nat. Methods **12**, 407–410 (2015).

63. P. Hajireza, A. Forbrich, and R. Zemp, "In-Vivo functional optical-resolution photoacoustic microscopy with stimulated Raman scattering fiber-laser source," Biomed. Opt. Express **5**, 539–46 (2014).

64. P. Hajireza, A. Forbrich, and R. J. Zemp, "Multifocus optical-resolution photoacoustic microscopy using stimulated Raman scattering and chromatic aberration.," Opt. Lett. **38**, 2711–3 (2013).

65. T. Buma, B. C. Wilkinson, and T. C. Sheehan, "Near-infrared spectroscopic photoacoustic microscopy using a multi-color fiber laser source," Biomed. Opt. Express **6**, 2819–29 (2015).

66. L. Wang, K. Maslov, J. Yao, B. Rao, and L. V Wang, "Fast voice-coil scanning optical-

resolution photoacoustic microscopy," Opt. Lett. **36**, 139–141 (2011).

67. L. Li, C. Yeh, S. Hu, L. V. L. Wang, B. T. Soetikno, R. Chen, Q. Zhou, K. K. Shung, K. I. Maslov, and L. V. L. Wang, "Fully motorized optical-resolution photoacoustic microscopy.," Opt. Lett. **39**, 2117–20 (2014).

68. Y. Wang and R. K. Wang, "Measurement of particle concentration in flow by statistical analyses of optical coherence tomography signals.," Opt. Lett. **36**, 2143–5 (2011).

69. S.-L. Chen, T. Ling, S.-W. Huang, H. Won Baac, and L. J. Guo, "Photoacoustic correlation spectroscopy and its application to low-speed flow measurement.," Opt. Lett. **35**, 1200–2 (2010).

70. B. Ning, N. Sun, R. Cao, R. Chen, K. Kirk Shung, J. A. Hossack, J.-M. Lee, Q. Zhou, and S. Hu, "Ultrasound-aided Multi-parametric Photoacoustic Microscopy of the Mouse Brain.," Sci. Rep. **5**, 18775 (2015).

71. W. J. Smith, *Modern Optical Engineering: The Design of Optical Systems*, Fourth Edi (New York: McGraw Hill, 2008).

72. J. Yao, K. I. Maslov, Y. Shi, L. A. Taber, and L. V Wang, "In vivo photoacoustic imaging of transverse blood flow by using Doppler broadening of bandwidth.," Opt. Lett. **35**, 1419–21 (2010).

73. T. Wang, R. Cao, B. Ning, A. J. Dixon, J. A. Hossack, A. L. Klibanov, Q. Zhou, A. Wang, and S. Hu, "All-optical photoacoustic microscopy based on plasmonic detection of broadband ultrasound," Appl. Phys. Lett. **107**, (2015).

74. Y. Liang, L. Jin, B.-O. Guan, and L. Wang, "2 MHz multi-wavelength pulsed laser for

functional photoacoustic microscopy," Opt. Lett. **42**, 1452 (2017).

75. D. J. Hausenloy, L. Candilio, R. Evans, C. Ariti, D. P. Jenkins, S. Kolvekar, R. Knight, G. Kunst, C. Laing, J. Nicholas, J. Pepper, S. Robertson, M. Xenou, T. Clayton, and D. M. Yellon, "Remote Ischemic Preconditioning and Outcomes of Cardiac Surgery," N. Engl. J. Med. (2015).

76. C. E. Murry, R. B. Jennings, and K. A. Reimer, "Preconditioning with ischemia: A delay of lethal cell injury in ischemic myocardium," Circulation (1986).

77. K. Przyklenk, B. Bauer, M. Ovize, R. A. Kloner, and P. Whittaker, "Regional ischemic “preconditioning” protects remote virgin myocardium from subsequent sustained coronary occlusion," Circulation (1993).

78. D. J. Hausenloy and D. M. Yellon, "Remote ischaemic preconditioning: Underlying mechanisms and clinical application," Cardiovasc. Res. (2008).

79. H. A. Jensen, S. Loukogeorgakis, F. Yannopoulos, E. Rimpiläinen, A. Petzold, H. Tuominen, P. Lepola, R. J. MacAllister, J. E. Deanfield, T. Mäkelä, K. Alestalo, K. Kiviluoma, V. Anttila, V. Tsang, and T. Juvonen, "Remote ischemic preconditioning protects the brain against injury after hypothermic circulatory arrest," Circulation (2011).

80. S. Hu, H. Dong, H. Zhang, S. Wang, L. Hou, S. Chen, J. Zhang, and L. Xiong, "Noninvasive limb remote ischemic preconditioning contributes neuroprotective effects via activation of adenosine A1 receptor and redox status after transient focal cerebral ischemia in rats," Brain Res. (2012).

81. Z. Wenwu, Z. Debing, C. Renwei, L. Jian, Y. Guangxian, L. Pingbo, and Z. Xinmin,

"Limb ischemic preconditioning reduces heart and lung injury after an open heart operation in infants," Pediatr. Cardiol. (2010).

82. A. Zarbock, C. Schmidt, H. Van Aken, C. Wempe, S. Martens, P. K. Zahn, B. Wolf, U. Goebel, C. I. Schwer, P. Rosenberger, H. Haeberle, D. Görlich, J. A. Kellum, M. Meersch, and RenalRIPC Investigators, "Effect of remote ischemic preconditioning on kidney injury among high-risk patients undergoing cardiac surgery: a randomized clinical trial.," JAMA (2015).

83. R. F. Zimmerman, P. U. Ezeanuna, J. C. Kane, C. D. Cleland, T. J. Kempananjappa, F. L. Lucas, and R. S. Kramer, "Ischemic preconditioning at a remote site prevents acute kidney injury in patients following cardiac surgery," Kidney Int. (2011).

84. S. P. Loukogeorgakis, A. T. Panagiotidou, M. W. Broadhead, A. Donald, J. E. Deanfield, and R. J. MacAllister, "Remote ischemic preconditioning provides early and late protection against endothelial ischemia-reperfusion injury in humans: Role of the autonomic nervous system," J. Am. Coll. Cardiol. (2005).

85. P. D. Addison, P. C. Neligan, H. Ashrafpour, A. Khan, A. Zhong, M. Moses, C. R. Forrest, and C. Y. Pang, "Noninvasive remote ischemic preconditioning for global protection of skeletal muscle against infarction.," Am. J. Physiol. Heart Circ. Physiol. (2003).

86. R. K. Kharbanda, U. M. Mortensen, P. A. White, S. B. Kristiansen, M. R. Schmidt, J. A. Hoschtitzky, M. Vogel, K. Sorensen, A. N. Redington, and R. MacAllister, "Transient limb ischemia induces remote ischemic preconditioning in vivo," Circulation (2002).

87. a Sharma, R. Jha, and B. Gupta, "Fiber-Optic Sensors Based on Surface Plasmon Resonance: A Comprehensive Review," Sensors Journal, IEEE **7**, 1118–1129 (2007).

88. J. Yao, L. Wang, C. Li, C. Zhang, and L. V. Wang, "Photoimprint photoacoustic microscopy for three-dimensional label-free subdiffraction imaging," Phys. Rev. Lett. **112**, (2014).

89. L. Wang, C. Zhang, and L. V. Wang, "Grueneisen relaxation photoacoustic microscopy," Phys. Rev. Lett. **113**, (2014).

90. R. L. Shelton, S. P. Mattison, and B. E. Applegate, "Volumetric imaging of erythrocytes using label-free multiphoton photoacoustic microscopy," J. Biophotonics (2014).

91. G. Langer, K.-D. Bouchal, H. Grün, P. Burgholzer, and T. Berer, "Two-photon absorption-induced photoacoustic imaging of Rhodamine B dyed polyethylene spheres using a femtosecond laser," Opt. Express (2013).

92. B. E. Urban, J. Yi, V. Yakovlev, and H. F. Zhang, "Investigating femtosecond-laser-induced two-photon photoacoustic generation," J. Biomed. Opt. (2014).

93. A. Danielli, K. Maslov, C. P. Favazza, J. Xia, and L. V. Wang, "Nonlinear photoacoustic spectroscopy of hemoglobin," Appl. Phys. Lett. **106**, (2015).

94. A. Danielli, C. P. Favazza, K. Maslov, and L. V. Wang, "Picosecond absorption relaxation measured with nanosecond laser photoacoustics," Appl. Phys. Lett. (2010).

95. K. L. Bell, P. Hajireza, and R. J. Zemp, "Coherence-gated photoacoustic remote sensing microscopy," Opt. Express **26**, 23689–23704 (2018).